

Observation of Nagaoka polarons in a Fermi–Hubbard quantum simulator

<https://doi.org/10.1038/s41586-024-07272-9>

Received: 23 August 2023

Accepted: 6 March 2024

Published online: 8 May 2024



Martin Lebrat^{1,6}, Muqing Xu^{1,6}, Lev Haldar Kendrick¹, Anant Kale¹, Youqi Gang¹, Pranav Seetharaman², Ivan Morera^{3,4,5}, Ehsan Khatami², Eugene Demler⁵ & Markus Greiner^{1✉}

Quantum interference can deeply alter the nature of many-body phases of matter¹. In the case of the Hubbard model, Nagaoka proved that introducing a single itinerant charge can transform a paramagnetic insulator into a ferromagnet through path interference^{2–4}. However, a microscopic observation of this kinetic magnetism induced by individually imaged dopants has been so far elusive. Here we demonstrate the emergence of Nagaoka polarons in a Hubbard system realized with strongly interacting fermions in a triangular optical lattice^{5,6}. Using quantum gas microscopy, we image these polarons as extended ferromagnetic bubbles around particle dopants arising from the local interplay of coherent dopant motion and spin exchange. By contrast, kinetic frustration due to the triangular geometry promotes antiferromagnetic polarons around hole dopants⁷. Our work augurs the exploration of exotic quantum phases driven by charge motion in strongly correlated systems and over sizes that are challenging for numerical simulation^{8–10}.

Ferromagnetism is an intrinsically quantum phenomenon with subtle origins. Conventionally, it arises from ferromagnetic exchange couplings originating from Coulomb interactions between electrons subject to the Pauli exclusion principle¹. This mechanism can, however, break down in the presence of strong electronic correlations. A prime example is provided by the Hubbard model, a minimal model capturing interactions between itinerant electrons on a lattice, relevant for a broad range of materials, including doped high-temperature superconducting cuprates¹¹. In this model, an antiferromagnetic ground state is favoured for experimentally relevant interactions at a filling of one particle per site.

Surprisingly, ferromagnetism can be recovered in the limit of infinitely strong interactions by adding one particle dopant to this half-filled state. As first shown by Nagaoka and Thouless^{2–4}, a ferromagnetic ground state arises from minimizing the kinetic energy of the dopant in a broad class of lattice geometries. Intuitively, Nagaoka ferromagnetism can be understood as the result of constructive interference between different paths the dopant may traverse in the presence of a ferromagnetic spin background (Fig. 1a). In any other background, dopant tunnelling may result in distinguishable spin configurations resulting in paramagnetic or antiferromagnetic states being less energetically favourable (Fig. 1b).

Nagaoka's exact result, however, relies on hypotheses that are challenging to meet in realistic materials. Its validity at finite interactions and beyond the single-dopant limit has been the focus of extensive theoretical work^{5,6,12–20}. Experimentally, evidence for Nagaoka ferromagnetism was shown on a 2×2 quantum dot plaquette²¹. Recent quantum simulations of the Hubbard model in moiré heterostructures^{22,23} and in cold-atom experiments²⁴ have mutually supported the existence of magnetic phases with kinetic origin. Despite these advances, signatures

of Nagaoka ferromagnetism due to individual dopants in an extended system have so far remained unobserved.

In this work, we experimentally demonstrate the emergence of Nagaoka polarons with strongly interacting ultracold fermions in an optical lattice that pristinely realize the Hubbard model (Fig. 1c). These polarons appear as bubbles of enhanced ferromagnetic correlations over areas up to about 30 sites around individual particle dopants, which we image through in situ measurements of three-point correlation functions. These bubbles are bounded by antiferromagnetic superexchange occurring at finite interactions (Fig. 1a) and represent a generalization of Nagaoka's original arguments⁶. Key to our observations is a triangular optical lattice^{24–29}, in which kinetic magnetism is strongly enhanced because of the frustration of antiferromagnetic order and the presence of short-length loops¹⁶. As a result, it is expected to give rise to a variety of single- or few-dopant polaronic states^{30–32} that can be observed through spectroscopic^{33,34} or real-space measurements^{35–37}.

Furthermore, triangular lattices break particle–hole symmetry, which means that Nagaoka's theorem does not apply in the case of a single hole dopant. We, however, observe evidence for kinetic magnetism around hole dopants in the form of antiferromagnetic bubbles, in agreement with a seminal prediction by Haerter and Shastry⁷. This asymmetry with respect to doping sharply contrasts with magnetic polarons emerging from exchange-mediated interactions between the dopant and its spin environment^{38–41}, as investigated in previous cold-atom realizations of the two-dimensional square Hubbard model^{42–44}. Itinerant spin polarons exhibiting this particle–hole asymmetry have recently been observed with ultracold fermions in a triangular lattice⁴⁵.

Here we realize a frustrated Hubbard model by preparing a balanced mixture of ultracold fermionic lithium-6 atoms in the two lowest

¹Department of Physics, Harvard University, Cambridge, MA, USA. ²Department of Physics and Astronomy, San José State University, San Jose, CA, USA. ³Departament de Física Quàntica i Astrofísica, Universitat de Barcelona, Barcelona, Spain. ⁴Institut de Ciències del Cosmos, Universitat de Barcelona, Barcelona, Spain. ⁵Institute for Theoretical Physics, ETH Zurich, Zurich, Switzerland. ⁶These authors contributed equally: Martin Lebrat, Muqing Xu. ✉e-mail: mgreiner@g.harvard.edu

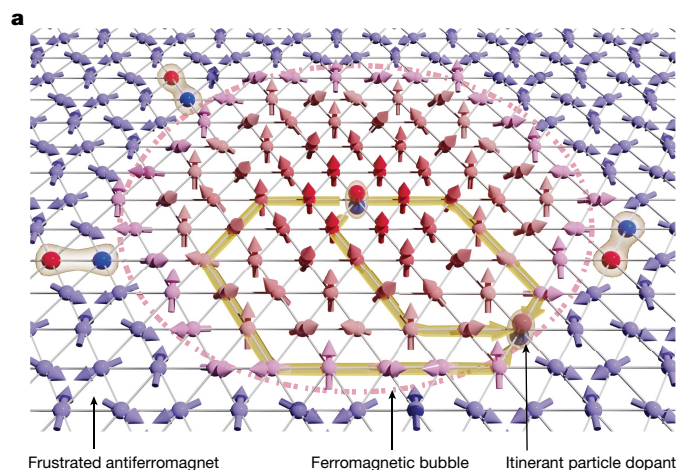
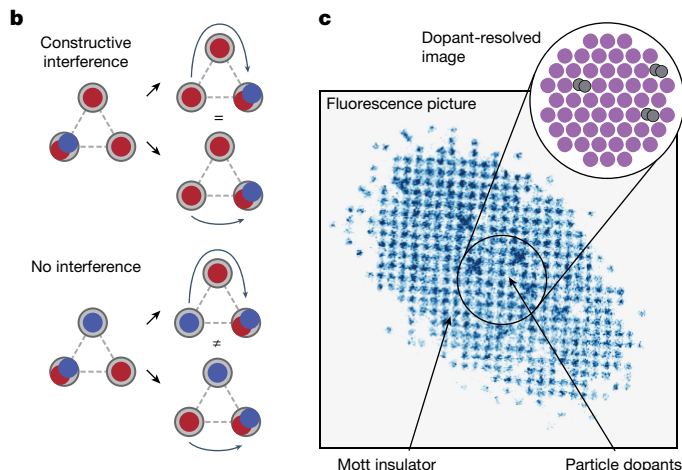


Fig. 1 | Nagaoka polarons in a Fermi–Hubbard quantum simulator. **a**, As it moves through a half-filled, Mott insulator described by the Hubbard model (purple spins), an itinerant particle dopant (doubly-occupied site at centre) favours spin alignment in its vicinity (pink circle), giving rise to a ferromagnetic polaron. Ferromagnetism of kinetic origin competes with superexchange coupling (red and blue pairs), which leads to antiferromagnetism away from the dopant. In the limit of infinite Hubbard interactions, the radius of the ferromagnetic polaron is expected to diverge and the ground state is a long-range ferromagnet, as shown by Nagaoka. **b**, Intuition behind kinetic magnetism: a ferromagnetic background enables constructive interference between paths



hyperfine states and adiabatically loading it into a triangular optical lattice²⁴. The tunnelling energy t and on-site interaction energy U that solely parameterize our Hubbard quantum simulator are tuned by changing the depth of the optical lattice and by controlling the magnetic field close to the broad Feshbach resonance of lithium-6 (see section ‘Sample preparation’). This enables us to tune the ratio U/t over more than one order of magnitude from the metallic regime, $U/t = 5.32(21)$, to the strongly interacting regime $U/t = 72(11)$, in which atoms form a large Mott insulator over 300–400 sites (Fig. 1c). Full dopant resolution is obtained by dynamically tuning the lattice geometry to a supersampling square lattice before fluorescence imaging (see section ‘Imaging procedure and fidelities’).

Nagaoka polarons

We first investigate the regime of small particle doping above half-filling, close to the single-dopant limit required by Nagaoka’s theorem. At finite interactions U , antiferromagnetic correlations resulting from superexchange coupling $J = 4t^2/U$ can obscure the kinetic magnetism locally induced by dopants. A natural way to quantify this local effect is to measure a connected three-point correlator that captures the amount of magnetism added by particle dopants to the spin background:

$$C_{\text{dss}}(\mathbf{r}_0; \mathbf{d}_1, \mathbf{d}_2) \equiv \frac{4}{N_{\text{dss}}} \langle \hat{d}_{\mathbf{r}_0} \hat{S}_{\mathbf{r}_0+\mathbf{d}_1}^z \hat{S}_{\mathbf{r}_0+\mathbf{d}_2}^z \rangle_c \quad (1)$$

where $\hat{d}_{\mathbf{r}}$ is the doublon occupation operator at site \mathbf{r} , $\hat{S}_{\mathbf{r}}^z$ is the projection of the local spin operator along the quantization axis, N_{dss} is the marginal probability to measure a doublon at site \mathbf{r}_0 and single spins at sites $\mathbf{r}_0 + \mathbf{d}_1$ and $\mathbf{r}_0 + \mathbf{d}_2$ (see section ‘Correlation functions’). Here and in the following, we measure $C_{\text{dss}}(\mathbf{r}_0; \mathbf{d}_1, \mathbf{d}_2)$ for pairs of nearest-neighbour spins, $|\mathbf{d}_2 - \mathbf{d}_1| = 1$, and radially average it over all pairs at the same distance $|\mathbf{d}| = (|\mathbf{d}_1 + \mathbf{d}_2|)/2$ from a particle dopant. Furthermore, it is averaged over a contiguous area of our experimental sample, including all sites \mathbf{r}_0 at or above half-filling.

We show the magnetism induced by a particle dopant on its surrounding spins in spatial maps of the three-point correlator $C_{\text{dss}}(|\mathbf{d}|)$

taken by the dopant, thereby lowering its kinetic energy. Conversely, different paths in a non-polarized background may lead to different spin configurations and reduce quantum interference. **c**, We realize the Hubbard model with tunable interaction and tunnelling by loading up to about 400 fermionic ^6Li atoms in a triangular optical lattice. Geometric frustration introduced by the triangular geometry facilitates kinetic ferromagnetism by suppressing superexchange coupling. Particle dopants are imaged at the single-site level (inset) after adiabatically changing the lattice geometry to a supersampling square lattice (shown in the experimental fluorescence picture; see section ‘Imaging procedure and fidelities’).

in Fig. 2a. At interaction strength $U/t = 5.5(1.0)$ for which the system is metallic, spin correlations are positive at the shortest distance from the particle dopant. These correlations show a damped oscillation between positive and negative values at longer distances, reminiscent of Friedel oscillations found in Fermi liquids. This behaviour is suppressed and finally vanishes as interaction strength increases. We find that correlations farther from the dopant also turn significantly positive up to a distance $|\mathbf{d}| = 2.5$ at the strongest interaction $U/t = 72(11)$ (Fig. 2b). These positive correlations form a ferromagnetic bubble covering an area of about 30 sites.

We interpret these bubbles of enhanced ferromagnetic correlations as Nagaoka polarons, resulting from mobile particle dopants locally polarizing the antiferromagnetic spin background. Initially discussed in the context of the stability of the long-range ferromagnetic state⁵, these polarons have been found in the ground state of the square t – J model in density-matrix renormalization group studies⁶. On the basis of variational arguments^{1,6}, the radius of the polaron is predicted to weakly scale with interactions as $R_N \sim (t/J)^{1/4} = \mathcal{O}(1)$, which is consistent with an increase in the number of positive correlators C_{dss} with U/t .

Owing to the confinement potential inherent to our trapping laser beams, our region of interest shows a slow spatial variation of the density n between 0.95 and about 1.2. We expect these inhomogeneities to average out the magnitude of the measured correlations and possibly underestimate their range, which makes it difficult to quantitatively estimate the polaron radius. Furthermore, numerical simulations show an overall decrease in the range of the correlations with doping, which is consistent with it being limited by the average distance between dopants (see section ‘Numerical methods’ and Extended Data Fig. 3).

As the interaction strength U/t is increased, experimental temperatures T remain smaller than the tunnelling energy t (see section ‘Calibration of t , U and T ’). They, however, exceed the superexchange energy $J = 4t^2/U$ that determines the magnetic properties of the Hubbard model at half-filling (Fig. 2c). The persistence of the observed ferromagnetic correlations at large distances in this temperature regime, therefore, confirms their kinetic origin.

The positive $C_{\text{dss}}(|\mathbf{d}| = \sqrt{3}/2)$ on the lattice bonds closest to the particle dopant are robust over a wide experimental range of interactions U/t

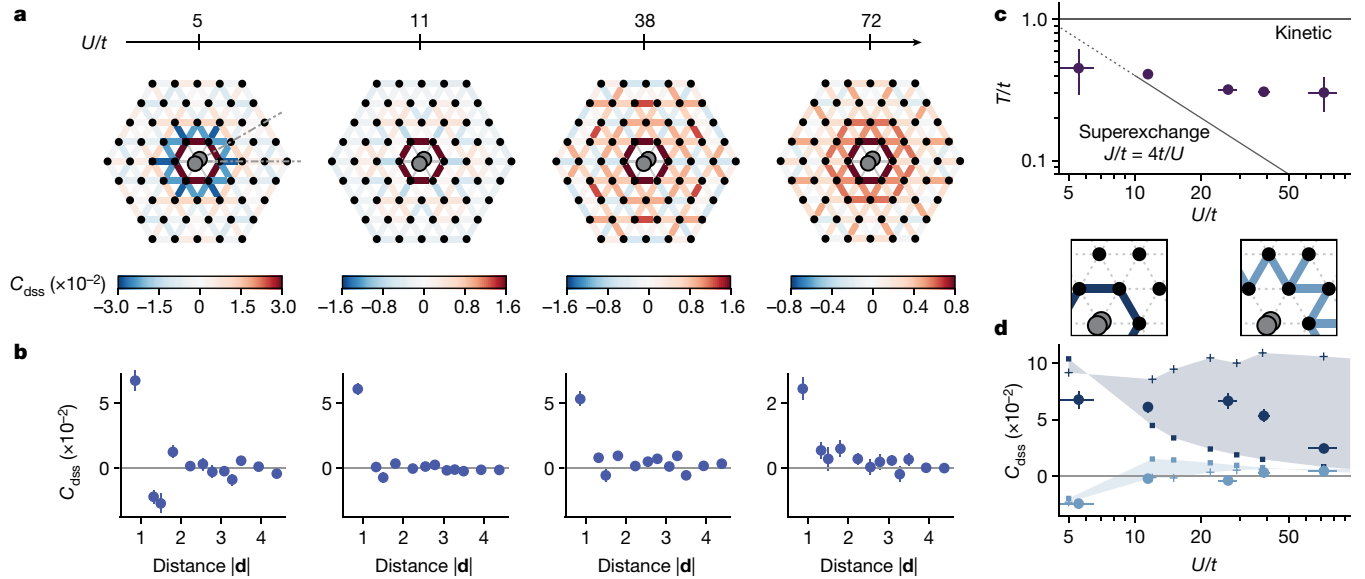


Fig. 2 | Emergence of Nagaoka polarons around particle dopants. **a**, Quantum gas microscopy enables us to directly investigate how a single dopant affects its spin environment. We observe the resulting ferromagnetic Nagaoka polaron around single doublon dopants by extracting the connected doublon–spin–spin correlation function $C_{\text{dss}}(|\mathbf{d}|)$ from quantum snapshots. The radius of the ferromagnetic bubble increases when increasing the interaction strength from $U/t = 5.5(1.0)$ to $72(11)$. The three-point correlations are averaged over lattice sites with filling larger than 0.95, then bond-averaged according to the spatial symmetries of the triangular lattice, which contains the two reflections indicated with dashed-dotted lines in the leftmost panel. **b**, The correlations C_{dss} are significantly positive up to a distance $|\mathbf{d}| = 2.5$ from the doubly-occupied site at $U/t = 72(11)$. Bonds within a radial distance of 0.15 are averaged together. Here and in the following, error bars indicate the 1σ confidence interval.

c, Increasing U suppresses the superexchange energy $J = 4t^2/U$ that determines the magnetic properties of the Hubbard model at half-filling. Our experimental temperatures T in the Mott insulating regime exceed this energy scale while remaining smaller than the tunnelling energy t , which strongly points to the kinetic origin of the observed magnetic correlations. **d**, Strong quantum interference on triangular plaquettes results in positive correlations C_{dss} at the shortest distance $|\mathbf{d}| = \sqrt{3}/2$ over a wide range of interactions U/t (dark-blue circles; see section ‘Toy model on a triangular plaquette’), whereas the sign of the correlator averaged on the next-nearest bonds $|\mathbf{d}| = \sqrt{7}/2$ and $|\mathbf{d}| = 3/2$ reverses between the Fermi liquid and the Mott insulating regimes (light-blue circles). These experimental data at short range are captured by numerical simulations performed at half-filling (squares) and 3% particle doping (crosses), performed at temperature $T/t = 0.5$ with DQMC for $U/t \leq 12$ and NLCE for $U/t \geq 15$.

from the metallic to the Mott insulating regime (Fig. 2d). This robustness may be attributed to the enhancement of quantum interference in the short length-three cycles that compose the triangular lattice. Neglecting interference over longer paths, the ground state of the Hubbard Hamiltonian on a three-site plaquette with one single particle dopant is a triplet state for any interaction strength $U > 0$ (see section ‘Toy model on a triangular plaquette’). By contrast, the ground state on a square plaquette is antiferromagnetic below a critical $U/t \sim 20$ (ref. 46), highlighting the tendency of ferromagnetism in short loops. The behaviour of the correlator C_{dss} both on the closest and next-closest bonds is qualitatively reproduced by numerical linked-cluster expansion (NLCE) simulations (Methods).

Kinetic magnetism

Triangular geometries not only give rise to geometric frustration of antiferromagnetic Heisenberg order but also to kinetic frustration of dopants, with important consequences on dopant-induced magnetism. A basic intuition can be gained by considering interference processes on a triangular plaquette (Fig. 3a), in which a dopant exchanges the position of two neighbouring spins on three consecutive tunnelling events. In contrast to a particle dopant, a hole dopant effectively has a negative tunnelling amplitude $-t$, which leads to destructive interference in a ferromagnetic background. However, constructive interference can be recovered if the neighbouring spin state is antisymmetric under exchange. From a kinetic energy perspective, hole dopants, therefore, favour singlet states with antiferromagnetic correlations. This asymmetry between particle and hole doping even holds in larger triangular systems: in the infinite U/t limit, Haerter and Shastry predicted the existence of 120° antiferromagnetic order around single

holes in the ground state⁷ that classically saturates the local magnetic moments⁴⁷, contrary to Heisenberg 120° antiferromagnetism driven by superexchange.

Experimentally, we observe antiferromagnetic polarons around single holes as shown by the hole–spin–spin correlator C_{hss} , defined similarly to C_{dss} in equation (1) and plotted in Fig. 3b, for interaction strength $U/t = 11.46(31)$ and densities $0.95 < n < 1.05$. The negative shortest-distance correlations are consistent with the results in ref. 7 and recent studies^{35,36}. We note that our imaging procedure prevents the measurement of C_{hss} between nearest-neighbour spins at larger distances from the hole analogous to Fig. 2a (see section ‘Correlation functions’).

After demonstrating the existence of kinetic magnetism carried by polarons close to half-filling, we now explore its evolution as the doping $\delta = n - 1$ is increased. We focus on correlations at the shortest distance $|\mathbf{d}| = \sqrt{3}/2$, and first show the total, connected dopant–spin–spin correlators $C_{\text{dss}}^{\text{tot}}$ and $C_{\text{hss}}^{\text{tot}}$ in Fig. 3c, equal to the correlators C_{dss} and C_{hss} without the uncorrelated normalization factor \mathcal{N}_{dss} . At interactions $U/t = 11.46(31)$, the non-normalized correlators show a linear doping dependence indicative of a regime in which the magnetism induced by each dopant is additive. In this regime, the visible antisymmetry close to half-filling $\delta = 0$ between $C_{\text{dss}}^{\text{tot}}$ for $\delta > 0$ and $C_{\text{hss}}^{\text{tot}}$ for $\delta < 0$ results from the Mott insulating nature of the parent system. Further away from half-filling, the non-normalized correlators decrease in magnitude because of the suppression of the local moments at large dopings but remain positive for doublon dopants and negative for hole dopants. We find good agreement between the experimental data and determinant quantum Monte Carlo (DQMC) simulations. We also show numerical simulations for the non-interacting and $U/t = \infty$ case (see section ‘Numerical methods’), highlighting the effect of interactions

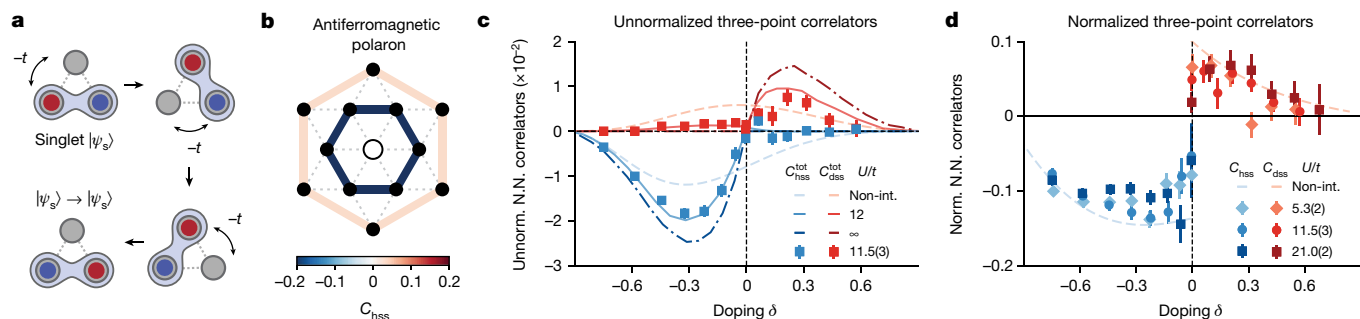


Fig. 3 | Antiferromagnetic polarons around holes and doping dependence of correlations. **a**, In contrast to particle dopants, hole dopants on a triangular plaquette favour antiferromagnetic correlations. As a hole dopant effectively has a negative tunnelling amplitude, it is kinetically frustrated on a triangular lattice with two aligned spins. However, it can delocalize by constructive interference if its neighbouring particles are in an antisymmetric spin state under exchange, that is, in a singlet state. **b**, Antiferromagnetic correlations are observed around hole dopants $C_{\text{hss}}(\mathbf{d}_i, \mathbf{d}_j)$, here averaged in a Mott insulator at interaction strength $U/t = 11.46(31)$ and temperature $T/t = 0.444(19)$. **c**, In the Mott insulating regime $U/t = 11.46(31)$, the symmetric nature of the ferromagnetic and antiferromagnetic polarons close to half-filling is visible as the linear doping dependence of the unnormalized connected hole–spin–spin correlator $C_{\text{hss}}^{\text{tot}}$ at dopings $\delta < 0$ and doublon–spin–spin correlator $C_{\text{dss}}^{\text{tot}}$ at dopings $\delta > 0$ between nearest neighbours ($|\mathbf{d}| = \sqrt{3}/2$). Away from half-filling, $C_{\text{hss}}^{\text{tot}}$ and $C_{\text{dss}}^{\text{tot}}$ decrease in

magnitude because of the decreasing local moments. The experimental data quantitatively agree with numerical simulations at $U/t = 12$ and $T/t = 0.5$. **d**, Kinetic magnetism at short distances from dopants is robust to doping and varying interaction strength after normalizing by the uncorrelated part of the correlator, as seen in the negative nearest-neighbour correlators C_{hss} and positive nearest-neighbour correlators C_{dss} . The value of the three-point correlators matches qualitatively the non-interacting calculation away from half-filling. The $U/t = 0, 12$ and ∞ numerics are computed at $T/t = 0.5$ using Wick's contractions, DQMC and FTLM, respectively (see section 'Numerical methods'). Unnorm., unnormalized; Norm., normalized; N.N., nearest neighbour; Non-int., non-interacting. In Extended Data Fig. 7, we show experimental and numerical data for the unnormalized three-point correlators for all three interaction strengths of Fig. 3 as a function of doping.

close to half-filling and the emergence of a linear regime at strong interactions.

Away from half-filling, the asymmetric particle- and hole-induced magnetism is robust to interaction strength, as shown in Fig. 3d with connected correlators normalized by N_{dss} or N_{hss} . We observe consistently negative short-range correlations C_{hss} around holes at all negative dopings $\delta < 0$, and positive short-range correlations C_{dss} around particle dopants up to $\delta = +0.5$. At dopings $|\delta| > 0.2$, non-interacting calculations at a temperature $T/t = 0.5$ show magnitudes similar to experimental data. Numerical simulations of C_{dss} from all methods also show quantitative agreement with each other at large particle doping (Extended Data Fig. 5), suggesting that the interaction dependence of the dopant–spin–spin correlations is the weakest in the highly doped regime.

Ferromagnetic transition at finite doping

The existence of Nagaoka polarons raises questions about their role in a possible ferromagnetic phase transition when dopant density is increased and polarons start to overlap (Fig. 4a). An analogous mechanism has been pointed out theoretically in disordered magnetic semiconductors, in which a ferromagnetic transition occurs through the percolation of localized ferromagnetic bubbles as the temperature is decreased⁴⁸.

In our experiment, the sign of the two-point spin correlation function between nearest-neighbour sites is suggestive of the ferromagnetic or antiferromagnetic nature of the system at equilibrium. In Fig. 4b, we plot the normalized two-point correlator

$$C_{\text{ss}}(\mathbf{r}; \mathbf{d}) \equiv \frac{4}{N_{\text{ss}}} \langle \hat{S}_{\mathbf{r}}^z \hat{S}_{\mathbf{r}+\mathbf{d}}^z \rangle_c \quad (2)$$

The correlator C_{ss} is measured as a function of doping at several interaction strengths in the temperature range $T/t = 0.40(4) - 0.74(13)$ (Methods and Extended Data Table 1). At half-filling ($\delta = 0$), superexchange interactions lead to an antiferromagnetic state ($C_{\text{ss}} < 0$). With particle doping ($\delta > 0$), however, this negative correlation is rapidly suppressed up to a critical doping δ_{FM} , at which it turns positive, consistent with a

scenario in which the proliferation of Nagaoka polarons drives a ferromagnetic transition. Conversely, with hole doping ($\delta < 0$), C_{ss} becomes even more negative than at half-filling, consistent with Haerter–Shastry polarons enhancing antiferromagnetism relative to the local moment⁴⁷. Neither of these trends is present in the equivalent correlator in the square lattice at comparable or larger interaction strengths, plotted in Fig. 4c. The latter quantity depends only weakly on doping, consistent with magnetism controlled mainly by the density of moments (that is, $\langle S^2 S^2 \rangle \propto (1 - |\delta|)^2$), in contrast to the kinetic magnetism evident in the triangular lattice.

Decreasing the superexchange energy $J = 4t^2/U$ by increasing U/t from 5.32(21) to 26.5(2.6) at similar temperatures suppresses superexchange magnetism while preserving kinetic magnetism. This effect is visible as an upward shift of the C_{ss} curve, whereas its slope stays roughly constant. The extreme limit of this effect is captured in finite-temperature Lanczos method (FTLM) simulations at $U/t = \infty$, $T/t = 0.6$, where $\delta_{\text{FM}} = 0$. The net result of this behaviour is a rapid reduction of the critical doping δ_{FM} towards half-filling (Fig. 4d) as interactions are increased. This trend is reminiscent of the existence of a ferromagnetic ground state for an infinitesimal positive doping of one hole in the Nagaoka limit $U/t \rightarrow \infty$, although the experimentally fitted δ_{FM} asymptotically reaches a small finite value, possibly as a consequence of the larger lattice depth and potential gradients associated with the trap curvature realized at the strongest interactions. Numerical simulations at fixed temperature $T/t = 0.6$ from the NLCE ($U/t = 5 - 100$; Methods) and FTLM ($U/t = 8$ to ∞ ; Methods) recover qualitatively similar δ_{FM} as U/t is increased, but with an asymptote approaching zero as $U/t \rightarrow \infty$.

Discussion and outlook

In this work, the enhancement of ferromagnetic correlations with interaction U around single particle dopants (Fig. 2a,b) and between nearest-neighbour spins (Fig. 4d) suggests that our finite-temperature system forms a precursor to a Nagaoka state at small, positive doping. The robust sign of both dopant–spin–spin (Fig. 3c,d) and spin–spin correlations (Fig. 4b) away from half-filling furthermore highlights the central role of coherent dopant motion in triangular geometries (Figs. 1a,b and 3a) to stabilize a ferromagnetic state at large particle

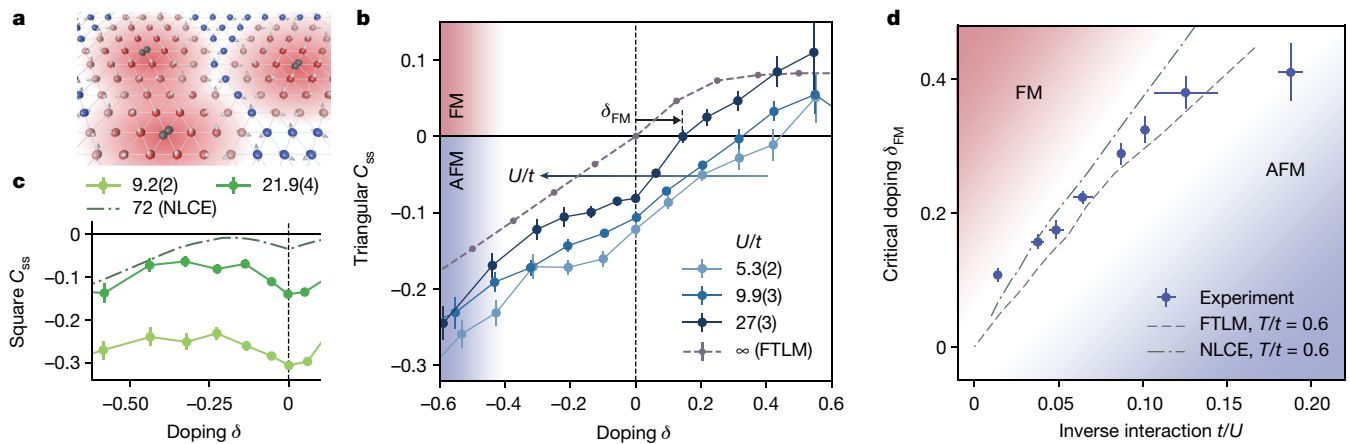


Fig. 4 | Critical doping for ferromagnetic correlations. **a**, Ferromagnetic tendencies increase with particle doping as ferromagnetic polarons start to overlap. **b**, A transition from an antiferromagnetic to a ferromagnetic short-range spin background is visible as a change of sign of the normalized nearest-neighbour spin–spin correlations C_{ss} in the triangular lattice at a critical doping δ_{FM} . Numerical simulations at $U = \infty$ and $T/t = 0.6$ by FTLM (Methods) exhibit a transition at half-filling consistent with Nagaoka’s and Haerter–Shastry’s pictures, in which magnetism is driven by a single dopant. **c**, No such transition occurs in experimental correlations from the square lattice at comparable U/t ,

doping and an antiferromagnetic state at large hole doping, in a regime in which spin-exchange magnetism is weak (Fig. 2d).

In the infinite U limit, long-range ferromagnetic order was previously shown to persist in the ground state of the triangular lattice up to remarkably large positive dopings^{3,16} compared with the square lattice^{17,19}. At finite interactions, the parent Mott insulating state at half-filling and zero temperature has been conjectured to show a transition from a 120° Néel ordered state to a quantum spin liquid below $U/t \approx 9$ – 10 , followed by an insulator to metal transition on further decreasing U/t (ref. 49). Doping the Mott insulator is expected to give rise to competing quantum phases, including chiral metals, spin density waves and superconducting states^{20,50,51}.

Experimentally, thermal fluctuations associated with our temperatures $T/t \geq 0.3$ prevent long-range order, and all measured observables are smooth functions of the interaction strength. Our lowest interactions $U/t \sim 5$ exhibit ferromagnetic nearest-neighbour spin correlations at critical dopings $\delta_{FM} > 0.3$ much larger than the strong interaction regime $U/t > 20$. In this weaker interaction regime, finite-doping ferromagnetism might be influenced by a Stoner instability. This hypothesis is supported by numerical density matrix renormalization group (DMRG) simulations shown in Extended Data Fig. 6 at $U/t = 20$ showing the formation of a long-range ferromagnetic ground state around a doping of 50%, at which the triangular lattice shows a van Hove singularity. Ferromagnetism in a triangular lattice could show a smooth crossover between the Stoner, mean-field regime at $U/t \approx 0$ and the Nagaoka, $U/t = \infty$, regime. Further theoretical and numerical studies as a function of lattice geometry and interaction can shed light on this crossover⁵².

Future work can further probe the existence of bound states mediated by kinetic frustration at finite polarization^{30,32,53,54} through measurements of spin susceptibility. These states have drawn interest from condensed-matter experiments with transition metal dichalcogenides, in which observations of kinetic magnetism and spin polarons have recently been reported^{22,23,55}. Our quantum simulator using ultracold atoms may help explain the mechanism of kinetic magnetism by providing a pristine realization of the triangular lattice Hubbard model and precisely tunable interactions. In the large doping regime, our platform could also investigate dopant pairing and superconductivity based on a ‘spin-bag’ mechanism⁵⁶. Our lowest experimental temperatures

nor even at $U/t = 72$ in correlations computed by NLCE at $T/t = 0.6$. **d**, The critical doping δ_{FM} decreases with increasing U/t , both in experimental data (blue), and in numerical simulations by FTLM (dashed line) and NLCE (dash-dotted line). This is consistent with the Nagaoka prediction of a ferromagnetic ground state for infinitesimal positive doping in the infinite limit $U/t \rightarrow \infty$. Red shading indicates regions of ferromagnetic correlations and blue shading indicates regions of antiferromagnetic correlations in the doping– t/U phase diagram. FM, ferromagnetic; AFM, antiferromagnetic.

$T/t \approx 0.3$, would allow the exploration of this phenomenon governed by tunnelling energy t , at interactions and dopings for which our finite-temperature simulations are challenging over large system sizes.

At weaker interactions for which spin exchange becomes dominant, multi-point correlation measurements of spin and density could also help reveal resonating-bond-solid states^{1,57}. Decreasing the temperature further may ultimately explain the nature of quantum spin liquid states and intriguing doped phases driven by frustration.

Online content

Any methods, additional references, Nature Portfolio reporting summaries, source data, extended data, supplementary information, acknowledgements, peer review information; details of author contributions and competing interests; and statements of data and code availability are available at <https://doi.org/10.1038/s41586-024-07272-9>.

- Auerbach, A. *Interacting Electrons and Quantum Magnetism* (Springer, 2012).
- Nagaoka, Y. Ferromagnetism in a narrow, almost half-filled s band. *Phys. Rev.* **147**, 392–405 (1966).
- Thouless, D. J. Exchange in solid ^3He and the Heisenberg Hamiltonian. *Proc. Phys. Soc.* **86**, 893 (1965).
- Tasaki, H. Extension of Nagaoka’s theorem on the large- U Hubbard model. *Phys. Rev. B* **40**, 9192–9193 (1989).
- Shastry, B. S., Krishnamurthy, H. R. & Anderson, P. W. Instability of the Nagaoka ferromagnetic state of the $U = \infty$ Hubbard model. *Phys. Rev. B* **41**, 2375–2379 (1990).
- White, S. R. & Affleck, I. Density matrix renormalization group analysis of the Nagaoka polaron in the two-dimensional t – J model. *Phys. Rev. B* **64**, 024411 (2001).
- Haerter, J. O. & Shastry, B. S. Kinetic antiferromagnetism in the triangular lattice. *Phys. Rev. Lett.* **95**, 087202 (2005).
- Anderson, P. W. Resonating valence bonds: a new kind of insulator?. *Mater. Res. Bull.* **8**, 153–160 (1973).
- Balents, L. Spin liquids in frustrated magnets. *Nature* **464**, 199–208 (2010).
- Zhou, Y., Kanoda, K. & Ng, T.-K. Quantum spin liquid states. *Rev. Mod. Phys.* **89**, 025003 (2017).
- Lee, P. A., Nagaoka, N. & Wen, X.-G. Doping a Mott insulator: physics of high-temperature superconductivity. *Rev. Mod. Phys.* **78**, 17–85 (2006).
- Doucot, B. & Wen, X. G. Instability of the Nagaoka state with more than one hole. *Phys. Rev. B* **40**, 2719 (1989).
- Fang, Y., Ruckenstein, A. E., Dagotto, E. & Schmitt-Rink, S. Holes in the infinite- U Hubbard model: instability of the Nagaoka state. *Phys. Rev. B* **40**, 7406–7409 (1989).
- Basile, A. G. & Elser, V. Stability of the ferromagnetic state with respect to a single spin flip: variational calculations for the $U = \infty$ Hubbard model on the square lattice. *Phys. Rev. B* **41**, 4842–4845 (1990).
- Barbieri, A., Riera, J. A. & Young, A. P. Stability of the saturated ferromagnetic state in the one-band Hubbard model. *Phys. Rev. B* **41**, 11697–11700 (1990).

16. Hanisch, T., Kleine, B., Ritzl, A. & Müller-Hartmann, E. Ferromagnetism in the Hubbard model: instability of the Nagaoka state on the triangular, honeycomb and kagome lattices. *Ann. Phys.* **507**, 303–328 (1995).
17. Wurth, P., Uhrig, G. & Müller-Hartmann, E. Ferromagnetism in the Hubbard model on the square lattice: Improved instability criterion for the Nagaoka state. *Ann. Phys.* **508**, 148–155 (1996).
18. Park, H., Haule, K., Marianetti, C. A. & Kotliar, G. Dynamical mean-field theory study of Nagaoka ferromagnetism. *Phys. Rev. B* **77**, 035107 (2008).
19. Liu, L., Yao, H., Berg, E., White, S. R. & Kivelson, S. A. Phases of the infinite U Hubbard model on square lattices. *Phys. Rev. Lett.* **108**, 126406 (2012).
20. Zhu, Z., Sheng, D. N. & Vishwanath, A. Doped Mott insulators in the triangular-lattice Hubbard model. *Phys. Rev. B* **105**, 205110 (2022).
21. Dehollain, J. P. et al. Nagaoka ferromagnetism observed in a quantum dot plaquette. *Nature* **579**, 528–533 (2020).
22. Tang, Y. et al. Simulation of Hubbard model physics in WSe_2/WS_2 moiré superlattices. *Nature* **579**, 353–358 (2020).
23. Ciorciaro, L. et al. Kinetic magnetism in triangular moiré materials. *Nature* **623**, 509–513 (2023).
24. Xu, M. et al. Frustration- and doping-induced magnetism in a Fermi–Hubbard simulator. *Nature* **620**, 971–976 (2023).
25. Struck, J. et al. Quantum simulation of frustrated classical magnetism in triangular optical lattices. *Science* **333**, 996–999 (2011).
26. Yamamoto, R., Ozawa, H., Nak, D. C., Nakamura, I. & Fukuhara, T. Single-site-resolved imaging of ultracold atoms in a triangular optical lattice. *New J. Phys.* **22**, 123028 (2020).
27. Yang, J., Liu, L., Mongkolkittichai, J. & Schauss, P. Site-resolved imaging of ultracold fermions in a triangular-lattice quantum gas microscope. *PRX Quantum* **2**, 020344 (2021).
28. Mongkolkittichai, J., Liu, L., Garwood, D., Yang, J. & Schauss, P. Quantum gas microscopy of fermionic triangular-lattice Mott insulators. *Phys. Rev. A* **108**, L061301 (2023).
29. Trisnadi, J., Zhang, M., Weiss, L. & Chin, C. Design and construction of a quantum matter synthesizer. *Rev. Sci. Instrum.* **93**, 083203 (2022).
30. Zhang, S.-S., Zhu, W. & Batista, C. D. Pairing from strong repulsion in triangular lattice Hubbard model. *Phys. Rev. B* **97**, 140507 (2018).
31. van de Kraats, J., Nielsen, K. K. & Bruun, G. M. Holes and magnetic polarons in a triangular lattice antiferromagnet. *Phys. Rev. B* **106**, 235143 (2022).
32. Davydova, M., Zhang, Y. & Fu, L. Itinerant spin polaron and metallic ferromagnetism in semiconductor moiré superlattices. *Phys. Rev. B* **107**, 224420 (2023).
33. Chen, S. A., Chen, Q. & Zhu, Z. Proposal for asymmetric photoemission and tunneling spectroscopies in quantum simulators of the triangular-lattice Fermi–Hubbard model. *Phys. Rev. B* **106**, 085138 (2022).
34. Morera, I., Weitenberg, C., Sengstock, K. & Demler, E. Exploring kinetically induced bound states in triangular lattices with ultracold atoms: spectroscopic approach. Preprint at <https://arxiv.org/abs/2312.00768> (2023).
35. Morera, I. et al. High-temperature kinetic magnetism in triangular lattices. *Phys. Rev. Res.* **5**, L022048 (2023).
36. Schlömer, H., Schollwöck, U., Bohrdt, A. & Grusdt, F. Kinetic-to-magnetic frustration crossover and linear confinement in the doped triangular t – J model. Preprint at <https://arxiv.org/abs/2305.02342> (2023).
37. Samajdar, R. & Bhatt, R. N. Nagaoka ferromagnetism in doped Hubbard models in optical lattices. Preprint at <https://arxiv.org/abs/2305.05683> (2023).
38. Brinkman, W. F. & Rice, T. M. Single-particle excitations in magnetic insulators. *Phys. Rev. B* **2**, 1324–1338 (1970).
39. Shraiman, B. I. & Siggia, E. D. Two-particle excitations in antiferromagnetic insulators. *Phys. Rev. Lett.* **60**, 740–743 (1988).
40. Sachdev, S. Hole motion in a quantum Néel state. *Phys. Rev. B* **39**, 12232–12247 (1989).
41. Grusdt, F. et al. Parton theory of magnetic polarons: mesonic resonances and signatures in dynamics. *Phys. Rev. X* **8**, 011046 (2018).
42. Koepsell, J. et al. Imaging magnetic polarons in the doped Fermi–Hubbard model. *Nature* **572**, 358–362 (2019).
43. Ji, G. et al. Coupling a mobile hole to an antiferromagnetic spin background: transient dynamics of a magnetic polaron. *Phys. Rev. X* **11**, 021022 (2021).
44. Koepsell, J. et al. Microscopic evolution of doped Mott insulators from polaronic metal to Fermi liquid. *Science* **374**, 82–86 (2021).
45. Prichard, M. L. et al. Directly imaging spin polarons in a kinetically frustrated Hubbard system. *Nature* <https://doi.org/10.1038/s41586-024-07356-6> (2024).
46. Yao, H., Tsai, W.-F. & Kivelson, S. A. Myriad phases of the checkerboard Hubbard model. *Phys. Rev. B* **76**, 161104 (2007).
47. Sposetti, C. N., Bravo, B., Trumper, A. E., Gazza, C. J. & Manuel, L. O. Classical antiferromagnetism in kinetically frustrated electronic models. *Phys. Rev. Lett.* **112**, 187204 (2014).
48. Kaminski, A. & Das Sarma, S. Polaron percolation in diluted magnetic semiconductors. *Phys. Rev. Lett.* **88**, 247202 (2002).
49. Szasz, A., Motruk, J., Zaletel, M. P. & Moore, J. E. Chiral spin liquid phase of the triangular lattice Hubbard model: a density matrix renormalization group study. *Phys. Rev. X* **10**, 021042 (2020).
50. Weber, C., Läuchli, A., Mila, F. & Giamarchi, T. Magnetism and superconductivity of strongly correlated electrons on the triangular lattice. *Phys. Rev. B* **73**, 014519 (2006).
51. Song, X.-Y., Vishwanath, A. & Zhang, Y.-H. Doping the chiral spin liquid: topological superconductor or chiral metal. *Phys. Rev. B* **103**, 165138 (2021).
52. Morera, I. & Demler, E. Itinerant magnetism and magnetic polarons in the triangular lattice Hubbard model. Preprint at <https://arxiv.org/abs/2402.14074> (2024).
53. Morera, I., Bohrdt, A., Ho, W. W. & Demler, E. Attraction from frustration in ladder systems. Preprint at <https://arxiv.org/abs/2106.09600> (2021).
54. Foutty, B. A. et al. Tunable spin and valley excitations of correlated insulators in γ -valley moiré bands. *Nat. Mater.* **22**, 731–736 (2023).
55. Tao, Z. et al. Observation of spin polarons in a frustrated moiré Hubbard system. *Nat. Phys.* <https://doi.org/10.1038/s41567-024-02434-y> (2024).
56. Schrieffer, J. R., Wen, X.-G. & Zhang, S.-C. Spin-bag mechanism of high-temperature superconductivity. *Phys. Rev. Lett.* **60**, 944 (1988).
57. Majumdar, C. K. & Ghosh, D. K. On Next-Nearest-Neighbor Interaction in Linear Chain. I. *J. Math. Phys.* **10**, 1388–1398 (1969).

Publisher's note Springer Nature remains neutral with regard to jurisdictional claims in published maps and institutional affiliations.

Springer Nature or its licensor (e.g. a society or other partner) holds exclusive rights to this article under a publishing agreement with the author(s) or other rightsholder(s); author self-archiving of the accepted manuscript version of this article is solely governed by the terms of such publishing agreement and applicable law.

© The Author(s), under exclusive licence to Springer Nature Limited 2024

Methods

Sample preparation

As in ref. 24, we prepare an ultracold, spin-balanced gas of ^6Li in the lowest two hyperfine states and load it into a triangular optical lattice formed by two interfering, actively phase-stabilized beams the intensities of which are independently controlled. We refer to these beams as X and Y . We tune the s-wave scattering length a_s of the lithium atoms by controlling the magnetic field in the vicinity of the broad Feshbach resonance at 832 G. Combining this and varying the final depth of the lattice allows access to a wide range of U/t values (see section ‘Calibration of t , U and T ’). In Extended Data Table 1, we report the lattice depth and tunnelling rate associated with each dataset. The lattices 1–6 are triangular lattices of varying depth, and 7 is a square lattice. To ensure the loading remains adiabatic, we use a ramp duration for each final lattice depth that is inversely proportional to the tunnelling rate t at the end of the loading ramp. We verify the adiabaticity of the lattice ramp by varying the ramp duration and checking the convergence of the density profile of the system as a function of distance from the trap centre. A digital micromirror device (DMD) is used to partially compensate for the harmonic confinement created by the Gaussian profile of the lattice beams. In most datasets a parabolic potential is projected from the DMD, although in a few datasets a hyperbolic pattern is projected to further compensate the potential. The potential is thus approximately harmonic in all datasets (see section ‘Trap uniformity and compensation’).

The experimental datasets thus produced are enumerated in Extended Data Table 1, together with the loading parameters, number of shots, interaction strength and temperature of each dataset and the figures each dataset appears in. The determination of the interaction strength and temperature is described in section ‘Calibration of t , U and T ’.

Imaging procedure and fidelities

To perform measurements on the system after loading it into the lattice, we first freeze the dynamics by quenching the lattice powers in 0.1 ms to $(V_X/E_R, V_Y/E_R) \approx (3.2, 40)$ (using the notation in ref. 24, where E_R is the lattice recoil energy) at which tunnelling is negligible. As in ref. 24, site-resolved fluorescence imaging is eventually performed on this frozen system in a separate, dedicated imaging lattice. In the present work, however, we take extra steps before the transfer to the imaging lattice to avoid the issue of parity projection, in which doubly-occupied sites seem to be empty because of light-assisted collisions during fluorescence imaging⁵⁸.

We achieve this by transferring the atoms from the triangular lattice to a square lattice with twice the number of sites, which converts doubly-occupied sites in the triangular lattice into adjacent pairs of singly-occupied sites in the square lattice. The transfer is performed by adiabatically ramping up an additional beam, which we call \bar{X} (Extended Data Fig. 1), to about $48E_R$ within 5 ms and ramping off the X lattice at a magnetic field at which the interaction between atoms is repulsive. \bar{X} copropagates with X but is detuned in frequency from X and Y by about 1.7 GHz. Owing to this large frequency offset, \bar{X} effectively does not interfere with X and Y , so that the handoff from $X + Y$ to $\bar{X} + Y$ doubles the number of sites ($\bar{X} + Y$ forms a ‘standard’ square lattice). The specific frequency of around 1.7 GHz is chosen to position the potential minima of $\bar{X} + Y$ symmetrically relative to those of $X + Y$ in each unit cell of the intermediate $X + \bar{X} + Y$ lattice. This choice minimizes differential potential offsets between the minima of $\bar{X} + Y$ during the handoff, which is necessary to ensure that the adiabatic splitting of doubly-occupied sites is robust. The choice of 1.7 GHz is then dictated by the wavelength of the lattice light (1,064 nm) and the distance to the retroreflection mirror (about 4.2 cm).

We obtain spin-resolved imaging by selectively removing atoms in one spin state with a resonant laser pulse, as in ref. 59. In the experiment, we use the two lowest hyperfine states of ^6Li , namely, the $(F=1/2, m_F=1/2)$ and $(F=1/2, m_F=-1/2)$ as the effective spin states $|\uparrow\rangle$ and $|\downarrow\rangle$. To prevent doubly-occupied sites from being affected by this pulse, before the splitting procedure we perform a radiofrequency Landau–Zener sweep to selectively transfer atoms in $|\downarrow\rangle$ on singly-occupied sites into the $(F=3/2, m_F=-3/2)$ ($|3\rangle$) state of the electronic state. To remove the $|\uparrow\rangle$ state, we perform an extra Landau–Zener sweep before transferring that exchanges $|\uparrow\rangle$ and $|\downarrow\rangle$ states on singly-occupied sites before transferring $|\downarrow\rangle$ to $|3\rangle$.

Doubly-occupied sites are not affected by these sweeps because of the interaction-induced shift of the hyperfine transition, which is typically about 30 kHz and hence much larger than the Rabi frequencies of the two sweeps (390 Hz and 180 Hz for the first and second sweeps, respectively). To ensure adiabaticity, we linearly sweep the frequency of the radiofrequency signal over a 15-kHz range centred on the resonance over a duration of 15 ms for the first sweep and 50 ms for the second sweep. This third spin state is then targeted for removal using a 10- μs resonant pulse⁵⁹ after the transfer to the imaging lattice (Extended Data Fig. 1).

We calibrate the fidelity of fluorescence imaging of the singly-occupied sites $F_s = 99\%$ as in ref. 24. To calibrate the fidelity $F_{d,\text{NR}}$ of doublons without the Landau–Zener transfer and spin removal, we load a cloud of atoms with a filling of $n = 2$ band insulating state in the centre of about 200 sites. We find the doublon detection fidelity to be $F_{d,\text{NR}} = 98\%$ after reconstruction. To characterize the doublon detection fidelity $F_{d,\uparrow}$ in the images with spin \uparrow removed and $F_{d,\downarrow}$ in the images with spin \downarrow removed, we apply the same Landau–Zener transfer and spin removal pulses used in data taking to the calibration sample with a band insulator core and find the fidelity to be $F_{d,\uparrow} = F_{d,\downarrow} = 95\%$.

Calibration of t , U and T

We obtain U/t and T/t in the triangular lattice by comparing experimental double-occupancy densities and spin correlations with DQMC and FTL simulations. For datasets from the square lattice, we use a similar procedure but compare with NLCE simulations from ref. 60. The results for U/t and T/t are listed in Extended Data Table 1.

As described in section ‘Determinant quantum Monte Carlo simulation’, we perform DQMC simulations of the triangular lattice Hubbard model on a mesh of μ , U and T , with simulation parameters described. At each point in the mesh, we compute the particle density $n(\mu, U, T)$, the double occupancy $d(\mu, U, T)$ and the nearest-neighbour spin correlator $C_{ss}(\mu, U, T)$. As U/t increases, DQMC becomes less stable because of the sign problem. However, for $U/t > 20$, we found the sign problem is absent at half-filling $n = 1$ and can be computed down to a temperature of $T/t = 0.3$.

To obtain U/t , we first perform linear interpolation on DQMC data using the experimentally measured double occupancy d and the nearest-neighbour spin correlator C_{ss} at half-filling. As we have a spatially varying atom density (see section ‘Trap uniformity and compensation’), these half-filling observables are determined by averaging over lattice sites with average density within $[0.97, 1.03]$, which is the most narrow range that includes enough lattice sites to reduce statistical noise. However, the values of U/t from interpolation still vary between datasets with the same lattice parameters due to statistical noise, and at $U/t > 20$, double occupancy d decreases to less than 1% and is more susceptible to imaging infidelity. Thus, we correct the interpolated value using the linear dependence of U on scattering length a_s (ref. 61).

For datasets with final calibrated $U/t < 20$, we take several other datasets with the same lattice depth and different magnetic fields, and we perform a linear fit of interpolated U/t on a_s , using values for a_s from ref. 62. For datasets with final calibrated $U/t > 20$, we take data at the same lattice depth but at a smaller magnetic field

Article

for which U/t is small and the measured double occupancy is still a faithful parameter to calibrate U/t , and then scale the interpolated U/t proportionally by a_s . This method produces the same U/t for the same lattice parameters and is robust against imaging infidelity.

To obtain T/t , we perform similar linear interpolation on DQMC data, but using the calibrated U/t and the experimentally measured nearest-neighbour spin correlator C_{ss} at half-filling. However, for $U/t > 35$, the sign problem of DQMC becomes severe even at half-filling, so we perform similar interpolation based on FTLM simulation of the t - J model, as described in section 'Finite-temperature Lanczos method simulation'.

In datasets from the square lattice, we obtain the experimental C_{ss} and d at half-filling as above. We then determine both U/t and T/t by linear interpolation on NLCE data from ref. 60.

We obtain the absolute value of the tunnelling t in Hz as described in ref. 24. We report the resulting tunnelling rates in Extended Data Table 1. Note that lattice 7 is a square lattice, whereas lattices 1–6 are triangular.

Correlation functions

Definition. The normalized, connected doublon–spin–spin correlator used in the main text is defined as

$$C_{dss}(\mathbf{r}_0; \mathbf{d}_1, \mathbf{d}_2) \equiv \frac{4}{\mathcal{N}_{dss}} \langle \hat{d}_{\mathbf{r}_0} \hat{S}_{\mathbf{r}_0+\mathbf{d}_1}^z \hat{S}_{\mathbf{r}_0+\mathbf{d}_2}^z \rangle_c \quad (3)$$

Here and in the following, the factor of 4 is used to normalize the $\hat{S}^z \hat{S}^z$ part of the correlator to one. The denominator is defined as $\mathcal{N}_{dss} = \langle d \rangle \langle p \rangle^2$, where $\langle d \rangle$ ($\langle p \rangle$) is the average probability for a site to be doubly (singly) occupied, and provides an upper bound for the three-point correlator. $\langle \dots \rangle_c$ denotes the connected part of the three-point correlation function, that is the difference between the doublon–spin–spin correlator and its disconnected parts. Under the assumption of a spin-balanced atomic mixture with total spin projection along z $\langle S^z \rangle = 0$, this connected correlator simplifies to

$$C_{dss}(\mathbf{r}_0; \mathbf{d}_1, \mathbf{d}_2) = \frac{4}{\mathcal{N}_{dss}} \langle \hat{d}_{\mathbf{r}_0} \hat{S}_{\mathbf{r}_0+\mathbf{d}_1}^z \hat{S}_{\mathbf{r}_0+\mathbf{d}_2}^z \rangle - C_{ss}(\mathbf{r}_0 + \mathbf{d}_1, \mathbf{r}_0 + \mathbf{d}_2). \quad (4)$$

It can be interpreted the amount of spin correlations added by doublons to the normalized spin correlation background:

$$C_{ss}(\mathbf{r}_1, \mathbf{r}_2) = \frac{4}{\mathcal{N}_{ss}} \langle \hat{S}_{\mathbf{r}_1}^z \hat{S}_{\mathbf{r}_2}^z \rangle \quad (5)$$

with normalization factor $\mathcal{N}_{ss} = \langle p \rangle^2$. Similarly, the normalized, connected hole–spin–spin correlator is defined as

$$C_{hss}(\mathbf{r}_0; \mathbf{d}_1, \mathbf{d}_2) \equiv \frac{4}{\mathcal{N}_{hss}} \langle \hat{h}_{\mathbf{r}_0} \hat{S}_{\mathbf{r}_0+\mathbf{d}_1}^z \hat{S}_{\mathbf{r}_0+\mathbf{d}_2}^z \rangle_c, \quad (6)$$

where $\mathcal{N}_{hss} = \langle h \rangle \langle p \rangle^2$, and $\langle h \rangle$ is the average probability for a site to be empty (hole).

In Fig. 3d, we show the nearest neighbour three-point correlator C_{dss} defined as

$$C_{dss}(\delta) \equiv \frac{1}{\mathcal{N}_{\Omega_\delta}} \sum_{\mathbf{r}_0 \in \Omega_\delta} \frac{1}{3} (C_{dss}(\mathbf{r}_0; \mathbf{e}_1, \mathbf{e}_2) + C_{dss}(\mathbf{r}_0; \mathbf{e}_2, \mathbf{e}_3) + C_{dss}(\mathbf{r}_0; \mathbf{e}_3, \mathbf{e}_1)), \quad (7)$$

where Ω_δ is a region with average doping level δ , $\mathcal{N}_{\Omega_\delta}$ is the number of lattice sites in this region, and \mathbf{e}_1 , \mathbf{e}_2 and \mathbf{e}_3 are the three unit vectors along the triangular lattice bonds. We similarly define the nearest neighbour hole–spin–spin correlator C_{hss} . In Fig. 3c, we also show the

non-normalized three-point correlators C_{dss}^{tot} and C_{hss}^{tot} , which are defined without the normalization factors \mathcal{N}_{dss} and \mathcal{N}_{hss} :

$$C_{dss}^{\text{tot}}(\mathbf{r}_0; \mathbf{d}_1, \mathbf{d}_2) \equiv 4 \langle \hat{d}_{\mathbf{r}_0} \hat{S}_{\mathbf{r}_0+\mathbf{d}_1}^z \hat{S}_{\mathbf{r}_0+\mathbf{d}_2}^z \rangle_c \quad (8)$$

In Fig. 4, we show the nearest-neighbour spin correlation C_{ss} defined as

$$C_{ss}(\delta) \equiv \frac{1}{\mathcal{N}_{\Omega_\delta}} \sum_{\mathbf{r}_0 \in \Omega_\delta} \frac{1}{3} (C_{ss}(\mathbf{r}_0, \mathbf{r}_0 + \mathbf{e}_1) + C_{ss}(\mathbf{r}_0, \mathbf{r}_0 + \mathbf{e}_2) + C_{ss}(\mathbf{r}_0, \mathbf{r}_0 + \mathbf{e}_3)), \quad (9)$$

where we average the correlator over the three equivalent lattice bonds and over a region of constant doping level.

Computation from experimental snapshots. As described in the previous section, we experimentally obtain three types of snapshot: (1) with no spin removal (NR); (2) after removing spin \uparrow ($R\uparrow$); and (3) after removing spin \downarrow ($R\downarrow$). Furthermore, in all three sets of images we can distinguish 0, 1 and 2 atoms per site, which we label as h , p and d , respectively. Extended Data Table 2 lists the site-resolved observed outcomes and the possible site occupations that map to the same measured outcome. With these three sets of images (even with parity-projected imaging), we can obtain connected two-point spin correlators $\langle S_i^z S_j^z \rangle_c$ for arbitrary sites i and j as demonstrated in our previous work⁵⁹. We repeat the formula below for clarity:

$$4 \langle S_i^z S_j^z \rangle_c = 2 \sum_{\sigma \in \{\uparrow, \downarrow\}} \langle p_i p_j \rangle_c^{(R\sigma)} - \langle p_i p_j \rangle_c^{(NR)}, \quad (10)$$

where $\langle \dots \rangle^{(NR)}$ refers to the expectation value over multiple images in which neither spin is removed, and $\langle \dots \rangle^{(R\sigma)}$ refers to the expectation value over images in which atoms in spin σ are removed.

With the addition of full-density resolution, we can also obtain connected three-point correlator doublon–spin–spin $\langle d_i S_j^z S_k^z \rangle_c$ for arbitrary sites i, j and k using the formula:

$$4 \langle d_i S_j^z S_k^z \rangle_c = 2 \sum_{\sigma \in \{\uparrow, \downarrow\}} 4 \langle d_i p_j p_k \rangle_c^{(R\sigma)} - 4 \langle d_i p_j p_k \rangle_c^{(NR)}. \quad (11)$$

This formula is a simple modification of equation (10), as we can uniquely identify doublons in each of the three sets of images as seen in Extended Data Table 2.

By contrast, because holes cannot be uniquely identified in our imaging scheme (a hole observed in a spin-removal image could be a hole or the spin that was removed), we cannot construct the hole–spin–spin correlator $\langle h_i S_j^z S_k^z \rangle_c$ for arbitrary sites i, j and k . However, we can still obtain a permutation-symmetrized combination of correlators $C_{hss}(i, j, k) = \sum_{(\bar{i}, \bar{j}, \bar{k}) \in (i, j, k)} \langle h_{\bar{i}} S_{\bar{j}}^z S_{\bar{k}}^z \rangle_c$ using the following formula:

$$C_{hss}(i, j, k) = \frac{4}{9} \sum_{(\bar{i}, \bar{j}, \bar{k}) \in (i, j, k)} \left(2 \sum_{\sigma \in \{\uparrow, \downarrow\}} \langle h_{\bar{i}} p_{\bar{j}} p_{\bar{k}} \rangle_c^{(R\sigma)} - \langle h_{\bar{i}} h_{\bar{j}} p_{\bar{k}} \rangle_c^{(R\sigma)} \right. \\ \left. + \langle h_{\bar{i}} p_{\bar{j}} p_{\bar{k}} \rangle_c^{(NR)} + 2 \langle h_{\bar{i}} h_{\bar{j}} p_{\bar{k}} \rangle_c^{(NR)} \right). \quad (12)$$

We can see how this formula works by writing out the first term of the connected correlator in the occupation basis. For convenience, we drop the site labels and imply averaging over cyclic permutation of the three sites.

$$4 \langle h S^z S^z \rangle = \langle h \uparrow \uparrow \rangle + \langle h \downarrow \downarrow \rangle - \langle h \uparrow \downarrow \rangle - \langle h \downarrow \uparrow \rangle. \quad (13)$$

Similarly writing out the three body terms from equation (12),

$$\begin{aligned}
& \frac{2}{3} \sum_{\sigma} (\langle hpp \rangle^{(R\sigma)} - \langle hhp \rangle^{(R\sigma)}) \\
& + \frac{1}{3} (\langle hpp \rangle^{(NR)} + 2\langle hhp \rangle^{(NR)}) \\
& = \frac{2}{3} (\langle \uparrow\downarrow\downarrow \rangle + \langle h\downarrow\downarrow \rangle + \langle \downarrow\uparrow\uparrow \rangle + \langle h\uparrow\uparrow \rangle) \\
& - \frac{2}{3} (\langle hh\downarrow \rangle + \langle h\uparrow\downarrow \rangle + \langle \uparrow h\downarrow \rangle + \langle \uparrow\uparrow\downarrow \rangle) \\
& + \langle hh\uparrow \rangle + \langle h\downarrow\uparrow \rangle + \langle \downarrow h\uparrow \rangle + \langle \downarrow\downarrow\uparrow \rangle) \\
& + \frac{1}{3} (\langle h\uparrow\uparrow \rangle + \langle h\uparrow\downarrow \rangle + \langle h\downarrow\uparrow \rangle + \langle h\downarrow\downarrow \rangle) \\
& + \frac{2}{3} (\langle hh\uparrow \rangle + \langle hh\downarrow \rangle) \\
& = \frac{2}{3} (\langle h\downarrow\downarrow \rangle + \langle h\uparrow\uparrow \rangle) \\
& - \frac{2}{3} (\langle h\uparrow\downarrow \rangle + \langle \uparrow h\downarrow \rangle + \langle h\downarrow\uparrow \rangle + \langle \downarrow h\uparrow \rangle) \\
& + \frac{1}{3} (\langle h\uparrow\uparrow \rangle + \langle h\uparrow\downarrow \rangle + \langle h\downarrow\uparrow \rangle + \langle h\downarrow\downarrow \rangle) \\
& = \langle h\uparrow\uparrow \rangle + \langle h\downarrow\downarrow \rangle - \langle h\uparrow\downarrow \rangle - \langle h\downarrow\uparrow \rangle,
\end{aligned} \tag{14}$$

where we used the cyclic permutation to cancel the terms in the last step. Similarly, in the two-body and on-site terms, appropriate terms get cancelled after cyclic permutation to give equation (12).

Trap uniformity and compensation

Trap curvature. Owing to the Gaussian envelope of the lattice beams and the additional light projected from the DMD, the atoms experience a spatially varying chemical potential. In a given dataset, we may estimate the resulting potential gradients by measuring the average experimental density $\langle n_r \rangle$ on each site, and using the equation of state computed in DQMC to extract the local chemical potential as $\mu(\mathbf{r}) = \mu_{\text{DQMC}}(\langle n_r \rangle, U, T)$ within the local density approximation. Here U and T are obtained as in section ‘Calibration of t , U and T ’, and the equation of state is inverted by linear interpolation on DQMC data from a range of μ values. We quantify the potential gradients by fitting parabolae to cuts of the local potential along the major and minor axes of the cloud, $\mu(r) = \mu_0 - \frac{1}{2}kr^2$. We report the fitted trap curvatures κ_{maj} and κ_{min} in Extended Data Table 3 for a representative subset of datasets. The uncertainties on these numbers account both for uncertainties on the site-resolved density $\langle n(\mathbf{r}) \rangle$ and on U and T . Typically κ_{maj} ranges from $0.03t/\text{sites}^2$ to $0.09t/\text{sites}^2$, whereas κ_{min} ranges from $0.3t/\text{sites}^2$ to $0.6t/\text{sites}^2$.

In datasets DS6, DS8 and DS10, in which we report (Fig. 3) three-point correlators at finite hole doping, we project a hyperbolic potential from the DMD to partially compensate for the minor axis confinement. The values of κ_{min} are thus correspondingly lower, for example, in DS10 and DS6 than in DS11 and DS7 (the analogous datasets for doublon doping in Fig. 3). This is done to reduce the local gradient in the hole-doped region of the trap, which can alter the value of correlation functions if it is too strong, as is discussed below. This compensation is unnecessary in the doublon-doped datasets because the doublon-doped region naturally occurs close to the trap centre.

Sensitivity to potential gradients. To estimate the sensitivity of the correlations reported in this paper to the potential gradients produced by the harmonic confinement, we perform FTLM simulations (see section ‘Finite-temperature Lanczos method simulation’), which we expect to qualitatively capture the relative effects of a potential gradient.

An example of the results of these calculations is shown in Extended Data Fig. 2, obtained from a $4 \times 3 t$ -J cluster at fixed $U/t = 30$ and $T/t = 0.5$. The left column plots the nearest-neighbour C_{ss} and smallest-triangle $C_{\text{hss, dss}}$ correlators (see section ‘Correlation functions’) as a function of

density at selected values of the gradient Δ (measured in t/site). The right column plots the same quantities as a function of the gradient strength at three example densities, chosen to be below, above or at half-filling. In this regime, we find the spin-spin correlations close to a Mott insulator remain robust even in the presence of gradients of about $10t/\text{site}$. The spin-spin correlations at finite doping and three-point correlations, however, are more strongly affected by gradients.

This difference in sensitivity to gradients in doped and undoped systems reflects the kinetic nature of the magnetism at finite doping. Dopant mobility is reduced in the presence of gradients because of the suppression of resonant tunnelling by site-to-site potential offsets. Potential gradients thus suppress kinetic magnetism, which results from the motion of dopants. By contrast, the virtual tunnelling responsible for superexchange interactions at half-filling in a Mott insulator is relatively unaffected by potential gradients (see, for example, refs. 63,64). As a result, magnetism at half-filling is much more robust to potential gradients than it is at finite doping.

Qualitatively, the most notable consequence of potential gradients is a strong reduction and even reversal of the hole-spin-spin correlator C_{hss} on the hole-doped side, which we address by specifically using trap compensation in the related dataset of Fig. 3. Quantitatively, we expect gradients to overall decrease the doublon-spin-spin correlators on the particle-doped side (Figs. 2 and 3), to decrease the magnitude of the spin-spin correlator C_{ss} on the hole-doped side and to increase the critical particle doping δ_{FM} at which the spin-spin correlator C_{ss} becomes ferromagnetic (Fig. 4).

Doping and interaction dependence of the doublon-spin-spin correlations

As described in the main text and in the section ‘Trap uniformity and compensation’, the region of interest used to compute the doublon-spin-spin correlation maps shown in Fig. 2 shows small spatial variations of the atom density. This leads to an averaging of the correlations C_{dss} over different doping values. To evaluate the exact doping dependence of the correlations, we perform numerical simulations at a reference temperature $T/t \approx 0.5$ (Extended Data Fig. 3). Overall, the magnitude of C_{dss} at large distances from the dopant is suppressed for dopings $\delta > 5\%$, which is generally expected to reduce the magnitude and range of the experimental correlations after averaging.

At small to moderate interactions $U/t = 5$ and 12 , we perform DQMC to obtain all dopant-spin-spin correlators on a 8×8 system size and for a large range of dopings. At $U/t = 5$, a Friedel-type oscillatory behaviour is visible as a function of distance from the doublon dopant or all the doping values shown in Extended Data Fig. 3a. The magnitude of the correlation is reduced for dopings $\delta > 20\%$. At $U/t = 12$, $C_{\text{dss}}(|\mathbf{d}|)$ values for $|\mathbf{d}| > 1$ start to be positive close to half-filling but turn negative at dopings $\delta \sim 2\%$ (Extended Data Fig. 3b). Notably, the second and third nearest neighbours turn negative at smaller doping than the fourth.

At larger interactions, we turn to NLCE simulations as the sign problem of DQMC becomes pronounced. We implemented $C_{\text{dss}}(|\mathbf{d}|)$ up to the fifth nearest neighbour from the doublon, with all further neighbours set to be 0 in the plot. At half-filling, all correlations are vanishing with interaction, in strong contrast with the particle-doped case (Extended Data Fig. 3c–e).

In Extended Data Fig. 4, we highlight the evolution of the first nearest neighbour C_{dss} and the average of the second and third nearest-neighbour correlations (as defined in Fig. 2), computed with NLCE across all interactions at doping values $\delta = 0$ and $\delta = 0.05$. At half-filling, the Hubbard model effectively maps to a Heisenberg model in the limit of large U/t and because the simulation is performed at constant temperature T/t , the effective increase in the temperature relative to superexchange T/J leads to a decrease in correlations. By contrast, at finite doping, the first nearest-neighbour correlator shows a very weak dependence on interaction strength, and the second turns from negative to positive at $U/t \sim 30$. This provides another confirmation that

Article

magnetism away from half-filling is not governed by superexchange/ but by the presence of mobile particle dopants with kinetic energy t .

At the largest interactions, doublon–spin–spin correlations also show a non-monotonic behaviour as doping is increased: both the range and the absolute value of the correlations increase at all five distances up to $\delta = 1\%$ doping and then start to decrease (up 8% at which NLCE starts to become unstable at $U/t = 100$), with a notably weak third nearest-neighbour correlator.

A difference between Fig. 2d and Extended Data Fig. 4 is the more abrupt decrease of the experimentally measured first nearest-neighbour at $U/t = 72(11)$. We attribute it to the experimental increase of the size of the Mott insulator region with interactions, which leads to a stronger weighting of weak correlations close to half-filling when performing a spatially uniform average.

Data analysis

In Fig. 2, three-point correlation functions are computed over all triplets of sites for which the average density is above 0.95. This corresponds to a spatial average over 123 sites at $U/t = 5.5(1.0)$ in the metallic regime and over 271–330 sites at the four other interactions in the Mott insulating regime. To eliminate slow shot-to-shot variations of the atom number that may introduce systematic shifts in the computed correlations, experimental images are post-selected within a window of ± 15 atoms away from the mean atom number for fully density-resolved images and ± 10 atoms for spin-resolved images (corresponding to relative fluctuations of about $\pm 5\%$ in both cases).

The data in Figs. 3 and 4 are post-selected with a window of ± 30 atoms in fully density-resolved images and ± 20 atoms in spin-resolved images. Experimental curves for doping are obtained by binning the sites of the lattice according to their measured density and averaging correlation functions in each bin, with typically 50 sites per bin. The experimental value of δ_{FM} in Fig. 4d is obtained from the zero of a linear fit to the curve thus obtained for C_{ss} in each dataset.

All error bars indicate the 1σ confidence interval obtained by using bootstrap sampling across all experimental snapshots of a given dataset with 100 randomly generated samples.

Comparison between numerical methods

We show the numerically computed normalized doublon–spin–spin and hole–spin–spin correlators in Extended Data Fig. 5a–d for finite temperature $T/t = 1$ as well as in the ground state. Surprisingly, we find an almost universal behaviour of the normalized doublon–spin–spin correlator above half-filling with very weak U/t dependence above doping $\delta > 0.1$. Similarly, we find weak U/t dependence of the normalized hole–spin–spin correlator below doping $\delta < -0.1$. However, as seen in Fig. 2 and Extended Data Fig. 3, the three-point correlators beyond the nearest neighbour vary significantly with interaction strength and show the range of the Nagaoka polaron increasing with interactions.

For completeness, we also show in Extended Data Fig. 5 the numerically computed bare doublon–spin–spin and hole–spin–spin correlator for nearest neighbours (Extended Data Fig. 5e,f) as well as the non-normalized, connected correlators (Extended Data Fig. 5g,h). The bare correlator doublon–spin–spin is defined as the first term in equation (4) without subtracting out the disconnected terms (similarly for the bare hole–spin–spin correlator). We note that the bare doublon–spin–spin correlator shows a sign change on going from low U/t to large U/t (similar to the spin–spin correlator), whereas the connected correlator is positive for all dopings and interaction strengths, indicating that the local spin correlations added by doublons is always ferromagnetic for all $U/t > 0$.

Doping-induced long-range ferromagnetism

The experimental observation of the Nagaoka polaron paves the way towards the detection of kinetic-energy-induced long-range ferromagnetism. Each doublon induces around it a small ferromagnetic

region, forming the Nagaoka polaron. When multiple doublons are injected into the system and the corresponding Nagaoka polarons start to overlap, a transition towards a long-range ferromagnet occurs. To show the formation of long-range ferromagnetism on doublon doping, we numerically compute the total spin squared at zero temperature,

$$\langle \mathbf{S}^2 \rangle = \sum_{ij} \langle \mathbf{S}_i \mathbf{S}_j \rangle. \quad (15)$$

Then, we associate a net total spin $\langle \mathbf{S} \rangle$ using the relation $\langle \mathbf{S}^2 \rangle = \langle \mathbf{S} \rangle (\langle \mathbf{S} \rangle + 1)$.

A long-range SU(2) ferromagnet is characterized by exhibiting a maximum total spin $\langle \mathbf{S} \rangle = (N_s - N_d)/2$, where N_s is the number of sites and N_d is the number of dopants $N_d = |\delta|N_s$. In Extended Data Fig. 6a, we show the dependence of the total spin as a function of the doping for a strong on-site interaction $U/t = 20$. We observe a transition towards a long-range ferromagnet at a critical doublon doping $\delta_{c1} \sim 0.45$. Moreover, the ferromagnetic state becomes unstable at a larger doublon doping $\delta_{c2} \sim 0.6 > \delta_{c1}$. Our numerical results support a scenario in which the overlap of multiple Nagaoka's polarons gives rise to the emergence of a long-range ferromagnetic state in the strongly interacting regime at zero temperature. Its interplay with other mechanisms (such as Stoner or flat-band ferromagnetism) as a function of the interaction U/t and geometry of the system is investigated in ref. 52.

Numerical methods

In the main text and the following, we define the Hubbard Hamiltonian as follows:

$$\hat{\mathcal{H}} = -t \sum_{\langle i,j \rangle, \sigma} (\hat{c}_{i,\sigma}^\dagger \hat{c}_{j,\sigma} + \text{h.c.}) + U \sum_i \hat{n}_{i,\uparrow} \hat{n}_{i,\downarrow} - \sum_{i,\sigma} \mu_i \hat{n}_{i,\sigma}$$

where $\hat{c}_{i,\sigma}^{(\dagger)}$ denotes the fermionic annihilation (creation) operator for spin $\sigma = \uparrow, \downarrow$ on lattice site i and h.c. denotes the Hermitian conjugate. The first sum is performed over pairs of nearest-neighbour sites $\langle i,j \rangle$. We chose the convention $t > 0$, leading to a negative tunnelling amplitude for particles and a positive tunnelling amplitude for holes.

Toy model on a triangular plaquette. Insights on the microscopic processes behind kinetic magnetism can be obtained by considering the previous Hamiltonian over a triangle formed by three sites $i = 0, 1$ and 2.

The case of a single hole dopant on a half-filled plaquette restricts the Hilbert space to Fock states consisting of two single spins or one doublon ($|0\rangle$ is the vacuum state with no particle):

$$|\sigma\sigma'\rangle = \hat{c}_{i+1,\sigma}^\dagger \hat{c}_{i+2,\sigma'}^\dagger |0\rangle \\ |D\rangle = \hat{c}_{i,\uparrow}^\dagger \hat{c}_{i,\downarrow}^\dagger |0\rangle.$$

Rewriting the two-spin states as triplet and singlet eigenstates of the total spin operator,

$$|T_i\rangle = (|\uparrow\downarrow\rangle + |\downarrow\uparrow\rangle)/\sqrt{2} \\ |S_i\rangle = (|\uparrow\downarrow\rangle - |\downarrow\uparrow\rangle)/\sqrt{2},$$

and furthermore transforming the Fock states into eigenstates of the translation operator, labelled by the normalized angular momentum $\ell = 0, \pm 1$:

$$|x_\ell\rangle = (|x_{\ell=0}\rangle + e^{i\ell\frac{2\pi}{3}} |x_{\ell=1}\rangle + e^{i\ell\frac{4\pi}{3}} |x_{\ell=2}\rangle)/\sqrt{3}$$

simplify the single-hole ground state and the first excited states to

$$|\phi_{\text{th}}^g\rangle \propto |s_{\ell=0}\rangle - \frac{1}{\sqrt{2}} \left(1 + \frac{E_{\text{g}}^{1h}}{2t} \right) |d_{\ell=0}\rangle \\ |\phi_{\text{th}}^e\rangle = |x_{\ell=\pm 1}\rangle, \quad x = \downarrow\downarrow, \uparrow\uparrow$$

with eigenenergies:

$$E_g^{\text{lh}} = -t + \frac{U}{2} - \sqrt{9t^2 + tU + U^2/4} \sim -2t - \frac{8t^2}{U} \quad \text{when } U \gg t$$

$$E_e^{\text{lh}} = -t$$

The eigenstates and eigenenergies of the single-particle-doped plaquette can be obtained through a particle-hole transformation $\hat{c} \leftrightarrow \hat{c}^\dagger$, $h \leftrightarrow d$, and with $|0\rangle$ the unit-filled state acting as a vacuum state for holes:

$$|\phi_{\text{ld}}^g\rangle = |x_{\ell=0}\rangle, \quad x = \downarrow\downarrow, t, \uparrow\uparrow$$

$$|\phi_{\text{ld}}^e\rangle \propto |s_{\ell=0}\rangle - \frac{1}{\sqrt{2}} \left(1 + \frac{E_e^{\text{lh}}}{t} \right) |h_{\ell=0}\rangle$$

with eigenenergies:

$$E_g^{\text{ld}} = -2t$$

$$E_e^{\text{ld}} = \frac{1}{2}(-t + U - \sqrt{9t^2 + tU + U^2/4}) \sim -t - \frac{2t^2}{U} \quad \text{when } U \gg t$$

The associated spectrum is shown in Extended Data Fig. 6b. For all positive interactions U , the ground state for one particle dopant is one of the three triplet states with angular momentum $\ell = 0$. By contrast, the ground state of a non-frustrated, square plaquette is ferromagnetic only past a critical $U > U_c \approx 18.6$ (ref. 46). For one hole dopant, the ground state is a superposition between a singlet and a doublon state with $\ell = 0$. In both cases, the lowest energy gap is equal to the kinetic energy t for $U = +\infty$. The energy of the predominantly singlet states is lowered at finite U by an energy proportional to the spin exchange coupling $J = 4t^2/U$, whereas triplet states are unaffected.

Finite-temperature Lanczos method simulation. We can compute the thermal expectation value $\langle A \rangle_\beta = \text{Tr}(e^{-\beta H} A) / \text{Tr}(e^{-\beta H})$ of arbitrary operators A at inverse temperature $\beta = 1/T$ and with Hamiltonian H on finite-sized clusters using FTLM^{65,66}. The Lanczos method involves starting from a random state $|r\rangle$ and finding a set of M basis vectors in which the Hamiltonian can be efficiently diagonalized yielding Lanczos approximate eigenvectors $|\psi_i\rangle$ and eigenvalues ϵ_i , for $i = 1, \dots, M$, allowing us to evaluate matrix elements of the form $\langle r | H^m A | r \rangle$ as long as $m < M$. Thermal expectation values can be constructed from these matrix elements as

$$\begin{aligned} \text{Tr}(e^{-\beta H} A) &\approx \sum_{m=0}^M \frac{(-\beta)^m}{m!} \text{Tr}(H^m A) \\ &\approx \sum_{m=0}^M \frac{(-\beta)^m}{m!} \frac{\dim(H)}{R} \sum_r^R \langle r | H^m A | r \rangle, \end{aligned}$$

where the first approximation comes from truncating the Taylor expansion in β to order M leading to error on the order $O(\beta^{M+1})$, whereas the second approximation comes from using $R < \dim(H)$ states to evaluate the trace that leads to a relative statistical error of the order $O(1/\sqrt{RZ})$ (ref. 66), which can be decreased by increased sampling (Z is the partition function, $Z = \text{Tr}(e^{-\beta H})$). In all the simulations, we use an order $M = 75$ Lanczos decomposition, which is typically enough to converge the ground state energy, and use $R = 200$ samples in each of the N_{total} and S_{total}^z symmetry sectors.

We write the Hamiltonian and operators in the Fock basis and work in the S_{total}^z conserving sectors as described in ref. 67. In Figs. 3d and 4b, we use the t - J Hamiltonian (including the three-site terms)⁶⁸ with $J = 4t^2/U$ to simulate the effects of large interaction strength, including

$U/t = \infty$. The restricted Hilbert space of the t - J model allows us to reach a system size of 4×4 sites with $\dim(H)_{\text{max}} \sim 2 \times 10^6$. The limited system size introduces some finite-size effects that can be seen when comparing simulations on 3×3 , 4×3 and 4×4 sites, and also when comparing against other numerical methods such as DQMC on 8×8 sites and NLCE simulations.

Non-interacting calculations. In a non-interacting Hubbard system, by Wick's theorem, the thermal expectation of any operator written as a product of the fermionic creation and annihilation operators can be evaluated by taking an appropriate sum over all possible contractions of these operators⁶⁹. This sum may be efficiently computed as the determinant of a matrix in which the entries are set from the non-interacting Green's function (as discussed, for example, in ref. 70). We use this technique to compute the correlation functions discussed in the section 'Correlation functions' for arbitrary μ and T values. For each μ and T , we compute the non-interacting Green's function for the triangular Hubbard model on a 200×200 mesh in momentum space, using standard formulae⁶⁹, which we convert to real space through a fast Fourier transform. In the parameter regimes we access, this choice of mesh is large enough that finite-size effects are negligible. As we compute only equal-time correlators, we need to store only the equal-time Green's function. This Green's function is then used to fill the matrices whose determinants yield the Wick contractions.

Determinant quantum Monte Carlo simulation. We use the QUEST package⁷¹ to perform unbiased simulations of the Fermi-Hubbard model on a 8×8 triangular lattice using the DQMC algorithm. DQMC introduces a Hubbard-Stratonovich transformation to transform the interacting Hamiltonian to a non-interacting Hamiltonian only quadratic in fermionic operators, but involving a summation over the Hubbard-Stratonovich field. For a non-interacting system with $U/t = 0$, DQMC becomes exact and computes the non-interacting equal-time Green's function, similar to the previous section. For an interacting system, the summation over Hubbard-Stratonovich field is expressed as a classical Monte Carlo problem and can be computed. Thus the operators such as density and correlation functions can be decomposed again using Wick's theorem into the same expressions as non-interacting equal-time Green's functions and computed after performing the Hubbard-Stratonovich transformation.

We added the expression of three-point doublon-spin-spin and hole-spin-spin correlation functions into the QUEST package, which allows us to compute all combinations of (i, j, k) for $\langle d_i S_j^z S_k^z \rangle$ and $\langle h_i S_j^z S_k^z \rangle$, respectively. The original QUEST package already calculates the doublon density d , density n and two-point spin-spin correlation function $\langle S^z S^z \rangle$. We can combine these observables to compute the connected correlators. As in ref. 24, we use 5,000 warmup passes and 30,000 measurement passes for each run. At large U or low temperatures, the sign problem gets worse as we average over 10 runs initialized with a random seed. Trotterization error also will get worse at large U and we decrease the Trotter step size $t\Delta\tau = 0.02$ for $U/t \leq 15$ to $t\Delta\tau = 0.01$ for $U/t \approx 15-25$ and $t\Delta\tau = 0.005$ for $U/t \approx 25-40$. The values are chosen to make sure the Trotter error is smaller than the statistical error.

Numerical linked-cluster expansion. In the NLCE⁷², an extensive property of the lattice model in the thermodynamic limit is expressed in terms of contributions from all distinct connected (linked) finite clusters, up to a certain size, that can be embedded in the lattice. The method can be summarized as the following series for P , the extensive property per site in the thermodynamic limit,

$$P = \sum_c W_p(c), \quad (16)$$

where $W_p(c)$ is the contribution of cluster c to the property, calculated recursively starting from $c \equiv$ a single site, according to the inclusion–exclusion principle:

$$W_p(c) = p(c) - \sum_{s \subset c} W_p(s). \quad (17)$$

Here, $p(c)$ is the property calculated for cluster c using full diagonalization of the Hamiltonian matrix, and s runs over all subclusters of c (clusters obtained by removing different numbers of sites from c). In practice, clusters that are related by point group symmetry operations of the underlying lattice are grouped together in the above sums. For details of the algorithm, including how to generate clusters and their subclusters for the series on a computer, see ref. 73.

We carry out this expansion for both the square lattice⁶⁰ and the triangular lattice Hubbard model to the ninth order, which means we work with clusters of a maximum of nine sites. We use the Wynn numerical resummation algorithm⁷³ with three and four cycles of improvement to extend the region of convergence of the series to lower temperatures, typically to $T/t = 0.6$ for the triangular lattice around half-filling and use their agreement as an indicator of convergence.

Density-matrix renormalization group. The ground state DMRG simulations are performed using TeNPy⁷⁴ with maximum bond dimension $\chi = 2,000$ on cylinders of width 4 (Fig. 4 and Extended Data Fig. 6a) and 6 (Extended Data Fig. 5). We perform two-site updates until we reach typical energy convergence of 10^{-6} and 10^{-4} in the entanglement entropy, followed by one-site updates to further improve the convergence. Observables are averaged over the system size, leading to larger error bars for a few points in the six-width simulations, in which our finite bond dimension $\chi \sim 2,000$ leads to artificial inhomogeneities.

Data availability

The datasets generated and analysed during this study are available from the corresponding author on reasonable request. Source data are provided with this paper.

Code availability

The codes used for the analysis are available from the corresponding author on reasonable request.

58. Bakr, W. S., Gillen, J. I., Peng, A., Fölling, S. & Greiner, M. A quantum gas microscope for detecting single atoms in a Hubbard-regime optical lattice. *Nature* **462**, 74–77 (2009).
59. Parsons, M. F. et al. Site-resolved measurement of the spin-correlation function in the Fermi-Hubbard model. *Science* **353**, 1253–1256 (2016).
60. Khatami, E. & Rigol, M. Thermodynamics of strongly interacting fermions in two-dimensional optical lattices. *Phys. Rev. A* **84**, 053611 (2011).

61. Bloch, I., Dalibard, J. & Zwerger, W. Many-body physics with ultracold gases. *Rev. Mod. Phys.* **80**, 885–964 (2008).
62. Zürn, G. et al. Precise characterization of ⁶Li Feshbach resonances using trap-sideband-resolved RF spectroscopy of weakly bound molecules. *Phys. Rev. Lett.* **110**, 135301 (2013).
63. Hirthe, S. et al. Magnetically mediated hole pairing in fermionic ladders of ultracold atoms. *Nature* **613**, 463–467 (2023).
64. Bohrdt, A., Homeier, L., Bloch, I., Demler, E. & Grusdt, F. Strong pairing in mixed-dimensional bilayer antiferromagnetic Mott insulators. *Nat. Phys.* **18**, 651–656 (2022).
65. Lanczos, C. An iteration method for the solution of the eigenvalue problem of linear differential and integral operators. *J. Res. Natl Bur. Stand.* **45**, 255–282 (1950).
66. Prelovsek, P. in *The Physics of Correlated Insulators, Metals, and Superconductors* (eds Pavarini, E. et al.) Ch. 7 (Forschungszentrum Jülich, Institute for Advanced Simulation, 2017).
67. Kale, A. et al. Schrieffer-Wolff transformations for experiments: dynamically suppressing virtual doublon-hole excitations in a Fermi-Hubbard simulator. *Phys. Rev. A* **106**, 012428 (2022).
68. MacDonald, A. H., Girvin, S. M. & Yoshioka, D. t/U expansion for the Hubbard model. *Phys. Rev. B* **37**, 9753–9756 (1988).
69. Abrikosov, A. A., Gorkov, L. P. & Dzyaloshinski, I. Y. *Methods of Quantum Field Theory in Statistical Physics* (Pergamon, 1965).
70. Rossi, R. Determinant diagrammatic monte carlo algorithm in the thermodynamic limit. *Phys. Rev. Lett.* **119**, 045701 (2017).
71. Varney, C. N. et al. Quantum monte carlo study of the two-dimensional fermion hubbard model. *Phys. Rev. B* **80**, 075116 (2009).
72. Rigol, M., Bryant, T. & Singh, R. R. P. Numerical linked-cluster approach to quantum lattice models. *Phys. Rev. Lett.* **97**, 187202 (2006).
73. Tang, B., Khatami, E. & Rigol, M. A short introduction to numerical linked-cluster expansions. *Comp. Phys. Commun.* **184**, 557–564 (2013).
74. Hauschild, J. & Pollmann, F. Efficient numerical simulations with tensor networks: Tensor Network Python (TeNPy). *SciPost Phys. Lect. Notes* <https://doi.org/10.21468/SciPostPhysLectNotes.5> (2018).

Acknowledgements We thank W. Bakr, T. Esslinger, B. S. Shastry, R. T. Scalettar, A. Bohrdt, F. Grusdt, H. Schlömer and R. Samajdar for their discussions. We acknowledge support from the Gordon and Betty Moore Foundation, grant no. GBMF-11521; the National Science Foundation (NSF), grants nos. PHY-1734011, OAC-1934598 and OAC-2118310; the ONR, grant no. N00014-18-1-2863; the DOE, QSA Lawrence Berkeley Lab award no. DE-AC02-05CH11231; QuEra, grant no. A444440; the ARO/AFOSR/ONR DURIP, grants nos. W911NF-20-1-0104 and W911NF-20-1-0163. M.L. acknowledges support from the Swiss National Science Foundation (SNSF) and the Max Planck/Harvard Research Center for Quantum Optics. L.H.K. and A.K. acknowledge support from the NSF Graduate Research Fellowship Program. Y.G. acknowledges support from the AWS Generation Q Fund at the Harvard Quantum Initiative. I.M. acknowledges support from grant no. PID2020-114626GB-I00 from the MICIN/AEI/10.13039/501100011033, Secretaria d'Universitats i Recerca del Departament d'Empresa i Coneixement de la Generalitat de Catalunya, cofunded by the European Union Regional Development Fund within the ERDF Operational Program of Catalunya (project no. QuantumCat, ref. 001-P-001644). E.K. and P.S. acknowledge support from the NSF under grant no. DMR-1918572. E.D. and I.M. acknowledge support from the SNSF project 200021_212899 and the NCCR SPIN of the SNSF. NLCE calculations were done on the Spartan high-performance computing facility at San José State University.

Author contributions M.L., M.X., L.H.K., A.K. and Y.G. performed the experiment and analysed the data. The numerical simulations were performed by M.X. (QMC), L.H.K. (non-interacting), A.K. (FTLM), P.S. (NLCE), I.M. (DMRG) and E.K. (NLCE). I.M., E.K. and E.D. developed the theoretical framework. M.G. supervised the study. All authors contributed to the interpretation of the results and production of the paper.

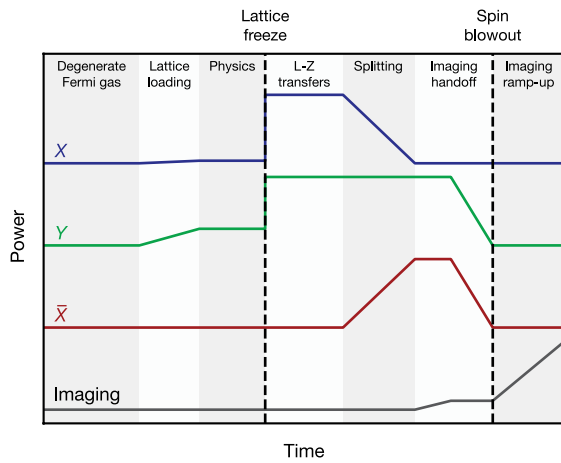
Competing interests M.G. is the co-founder and shareholder of QuEra Computing.

Additional information

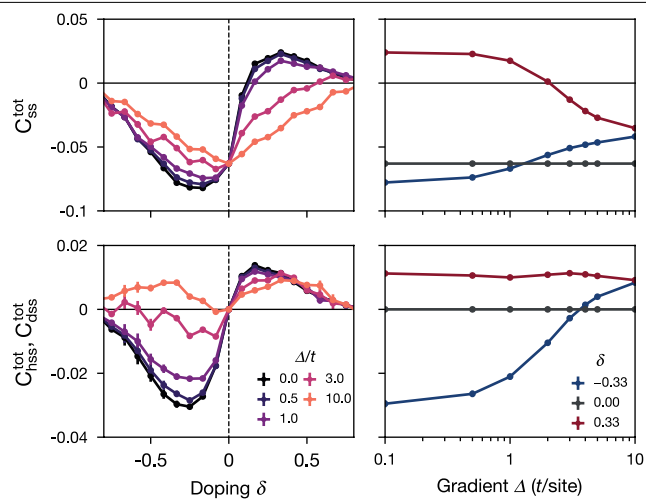
Correspondence and requests for materials should be addressed to Markus Greiner.

Peer review information Nature thanks Georg Bruun, Jae-yoon Choi and Zheng Zhu for their contribution to the peer review of this work.

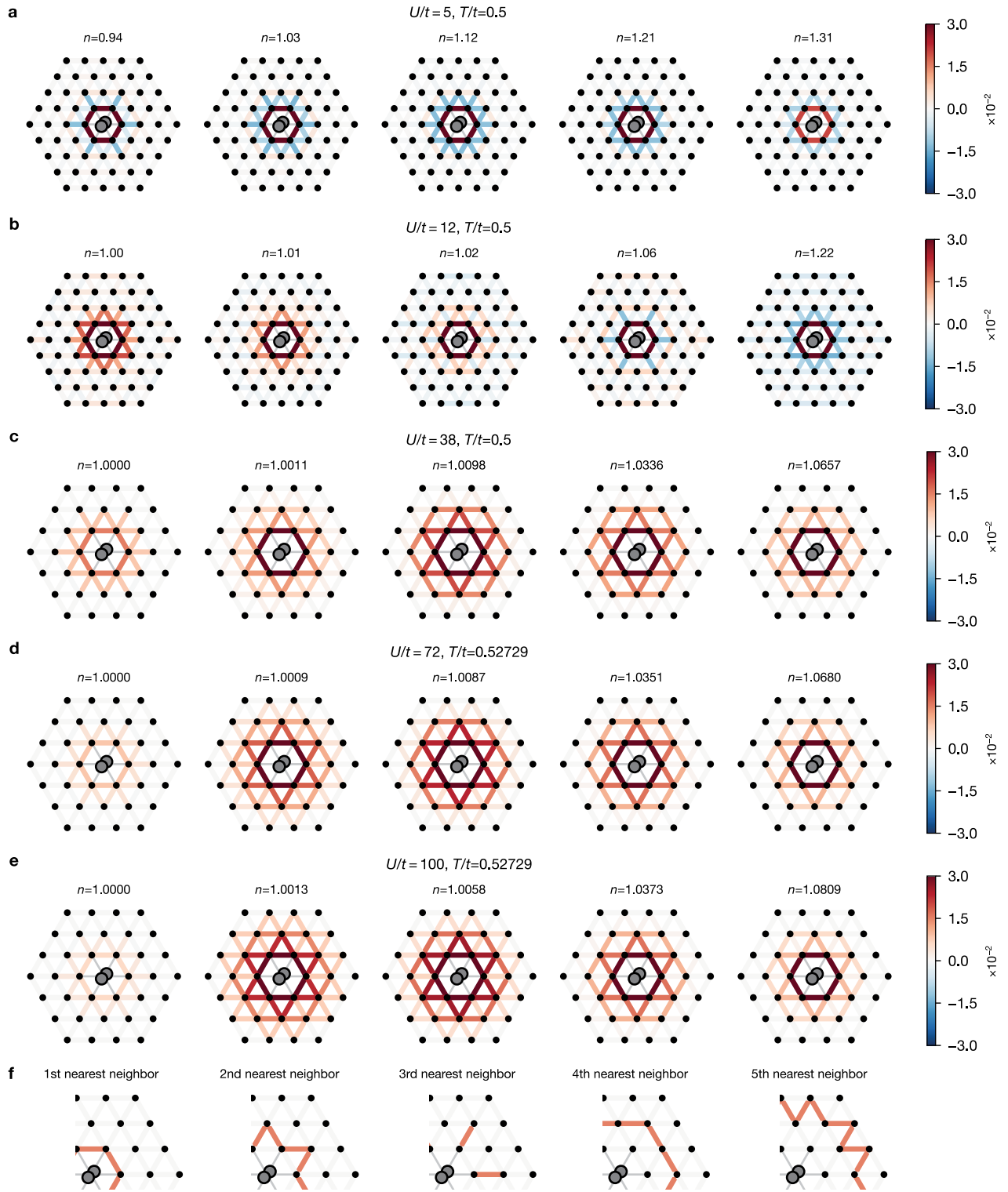
Reprints and permissions information is available at <http://www.nature.com/reprints>.



Extended Data Fig. 1 | Schematic of experimental sequence. A degenerate Fermi gas is loaded into a lattice formed by beams X and Y with a linear ramp of the lattice power. The lattice power is quenched to freeze tunneling. Radiofrequency Landau-Zener transfers are used in some shots to change the spin states on singly-occupied sites. Handing off from $X + Y$ to $\bar{X} + Y$ adiabatically doubles the unit cell, converting doubly-occupied sites to pairs of singly-occupied sites. Atoms are handed off to a separate imaging lattice, where a resonant laser is used in some shots to selectively remove one spin state.

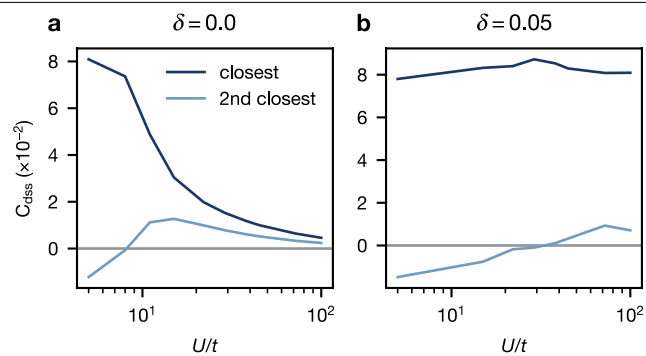


Extended Data Fig. 2 | Effect of potential gradients. Numerical simulation (FTLM) of the nearest-neighbour non-normalized spin-spin and hole-spin-spin (doublon-spin-spin) correlation functions in a $4 \times 3t - J$ cluster as a function of doping δ and gradient strength Δ , at fixed $U/t = 30$ and $T/t = 0.5$.

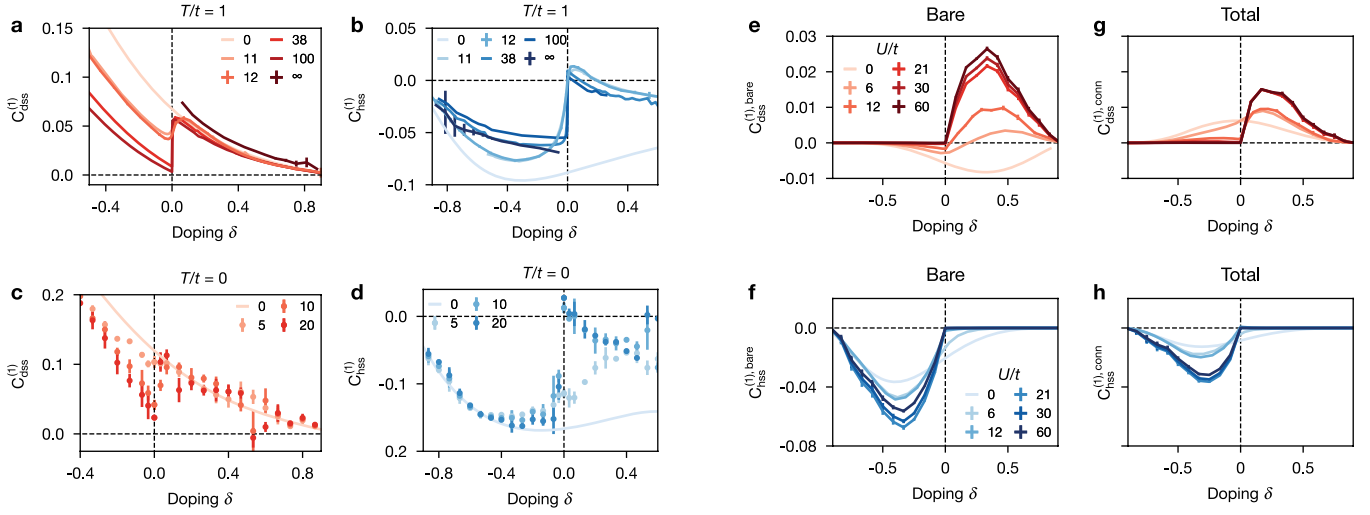


Extended Data Fig. 3 | Numerical simulation of doublon-spin-spin correlation map at different densities. We compute the connected doublon-spin-spin correlation function **a**, with DQMC at $U/t = 5$ and $T/t = 0.5$; **b**, with DQMC at $U/t = 12$ and $T/t = 0.5$; **c**, with NLCE at $U/t = 38$ and $T/t = 0.5$; **d**, with NLCE

at $U/t = 72$ and $T/t = 0.52729$; **e**, with NLCE at $U/t = 100$ and $T/t = 0.52729$. **f**, Definition of bonds averaged together in NLCE simulations. Bonds beyond fifth nearest-neighbor are not computed and set to zero in the plot.

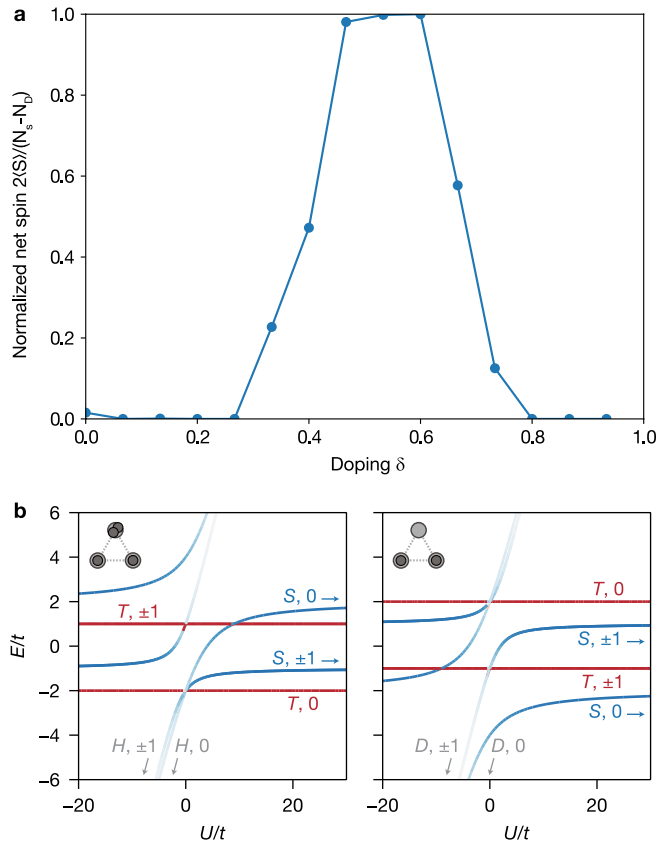


Extended Data Fig. 4 | NLCE closest and second-closest doublon-spin-spin correlations. Connected doublon-spin-spin correlator as a function of interaction strength, obtained from NLCE simulations at $T/t = 0.7$; **a**, at half-filling and **b**, at particle doping $\delta = 0.05$. See Fig. 2 for a definition of the correlators.



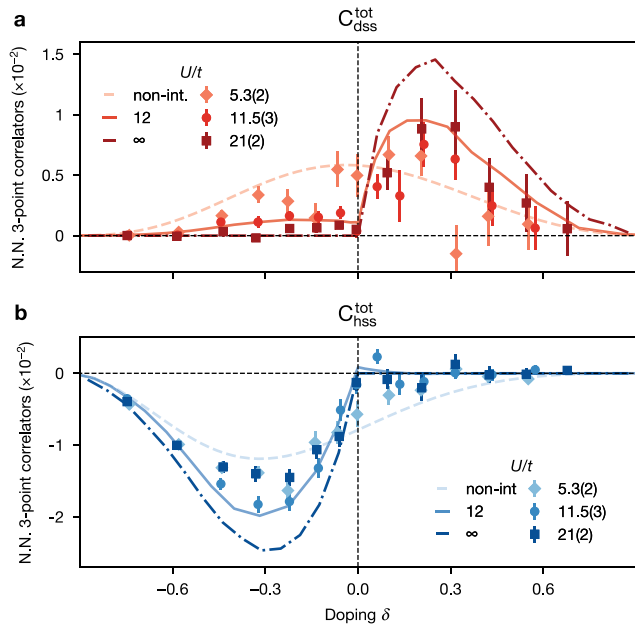
Extended Data Fig. 5 | Comparison of numerically computed three-point correlators as a function of doping and interaction strength. a to d, Comparison between **a, b**, finite-temperature, $T/t = 1$ correlators and **c, d**, ground-state correlators between nearest neighbors, normalized according to Eqs. (3), (4), (6) and (7) (see Fig. 3d). **a, c**, doublon-spin-spin correlators $C_{\text{dss}}^{(1)}$, showing an almost universal behavior above half-filling ($\delta > 0$) for the various interaction strengths. **b, d**, hole-spin-spin correlators $C_{\text{hss}}^{(1)}$. The $U/t = 0$ numerics

are computed using Wick's contraction, $U/t = 12$ using DQMC, $U/t = 11, 38, 100$ using NLCE, $U/t = \infty$ using FTLM, and $U/t = 5, 10, 20$ using DMRG. **e to h**, Comparison between **e, f**, bare correlators $C_{\text{dss, hss}}^{\text{bare}}$ and **g, h**, non-normalized correlators $C_{\text{dss, hss}}^{\text{tot}}$ (as defined in Eq. (8) and Fig. 3c). The $U/t = 0$ numerics are computed using Wick's contraction, $U/t = 6, 12$ using DQMC at $T/t = 0.5$, and $U/t > 20$ using FTLM. The errors in FTLM and DQMC are statistical while in DMRG they indicate the spatial variation of the correlators over the simulated system.



Extended Data Fig. 6 | Ferromagnetic state in ground-state simulations.

a, DMRG simulation of the net total spin $\langle S \rangle$ normalized by maximal spin as a function of doping δ , at $U/t = 20$ and zero temperature, showing the emergence of long-range ferromagnetism with doublon doping. **b**, Spectrum of the Hubbard Hamiltonian on a triangular plaquette. Eigenenergies are shown as a function of interaction strength U/t for one particle dopant (left) and one hole dopant (right). Labels show the nature of the state at infinite interaction $U/t = \pm\infty$ (S : singlet; T : triplet; H : one hole; D : one doublon) and its angular momentum $\ell = 0, \pm 1$ (see text for definitions). Colors indicate the sign and magnitude of the spin correlations.



Extended Data Fig. 7 | Extended data on doping dependence of three-point correlators. **a**, Doublon-spin-spin and **b**, hole-spin-spin correlation function on a triangular plaquette without normalization factor, see Eq. (8) for definition and Fig. 3 for details.

Extended Data Table 1 | Summary of experimental datasets

Dataset	Lattice	t_x (Hz)	t_y (Hz)	t' (Hz)	Ramp time (ms)	Field (G)	U/t	T/t	Shots	Figures
DS1	1	380(20)	360(20)	370(6)	160	585	6(1)	0.5(2)	389	2
DS2	2	283(17)	267(16)	283(6)	210	610	11.5(3)	0.409(7)	682	2
DS3	3	183(12)	172(11)	173(5)	330	610	27(3)	0.302(5)	582	2
DS4	4	138(10)	129(9)	134(4)	412	610	39(2)	0.306(2)	1074	2
DS5	5	86(7)	79(6)	83(3)	660	610	72(11)	0.30(8)	1876	2
DS6	2	283(17)	267(16)	283(6)	210	610	11.5(3)	0.44(2)	381	3
DS7	2	283(17)	267(16)	283(6)	210	610	11.5(3)	0.65(2)	259	3, 4
DS8	6	216(14)	203(13)	214(6)	250	610	21(2)	0.31(2)	199	3
DS9	6	216(14)	203(13)	214(6)	250	610	21(2)	0.50(6)	175	3, 4
DS10	2	283(17)	267(16)	283(6)	210	565	5.3(2)	0.58(8)	333	3
DS11	2	283(17)	267(16)	283(6)	210	565	5.3(2)	0.7(1)	309	3, 4
DS12	2	283(17)	267(16)	283(6)	210	600	9.9(3)	0.62(4)	267	4
DS13	3	183(12)	172(11)	173(5)	330	610	27(3)	0.40(4)	243	4
DS14	1	380(20)	360(20)	370(6)	160	607.5	8(1)	0.58(7)	200	4
DS15	6	216(14)	203(13)	214(6)	250	595	16(1)	0.40(2)	298	4
DS16	5	86(7)	79(6)	83(3)	660	610	72(11)	0.28(8)	1158	4
DS17	7	192(7)	175(7)	3.7(2)	400	570	9.2(2)	0.277(7)	199	4
DS18	7	192(7)	175(7)	3.7(2)	400	610	21.9(4)	0.6(1)	195	4

Note that DS6 is used in both Fig. 3b,d. For each value of U/t in Fig. 3d, the hole- and particle-doped curves are obtained from separate datasets (DS6, DS8, and DS10 are hole-doped). Datasets DS11, DS12, and DS13 appear in Fig. 4b.

Extended Data Table 2 | Summary of the density resolved and spin-removal imaging technique

Observed outcome	Possible occupation
$d^{(NR)}$	d
$d^{(R\uparrow)}$	d
$d^{(R\downarrow)}$	d
$p^{(NR)}$	\uparrow, \downarrow
$p^{(R\uparrow)}$	\downarrow
$p^{(R\downarrow)}$	\uparrow
$h^{(NR)}$	h
$h^{(R\uparrow)}$	h, \downarrow
$h^{(R\downarrow)}$	h, \downarrow

The left column lists all the site-resolved measured outcomes and the right column lists the possible site occupations that map to the same measured outcome.

Extended Data Table 3 | Trap curvature in a representative subset of datasets

Dataset	κ_{maj} (t/site ²)	κ_{min} (t/site ²)
DS1	0.036(3)	0.35(4)
DS6	0.085(4)	0.35(7)
DS7	0.060(5)	0.62(7)
DS10	0.068(3)	0.39(4)
DS11	0.053(3)	0.55(4)
DS12	0.043(3)	0.47(4)
DS14	0.036(7)	0.38(9)